Analysis of 3D Cloud Effects in OCO-2 XCO2 Retrievals

Steven. T. Massie[1], Heather Cronk[2], Aronne Merrelli[3], Christopher O'Dell[2], K. Sebastian Schmidt[1], Hong Chen[1], and David Baker[4]

[1]Laboratory for Atmospheric and Space Physics, University of Colorado, Boulder, Colorado, 80303, USA
[2]Colorado State University, Fort Collins, Colorado, 80523, USA
[3]Space Science and Engineering Center, University of Wisconsin-Madison, Madison,
10 Wisconsin, 53706, USA
[4]Cooperative Institute for Research in the Atmosphere, Colorado State University, Fort Collins, Colorado, 80523, USA

Correspondence to: Steven T Massie (Steven.Massie@lasp.colorado.edu)

Abstract. The presence of 3D cloud radiative effects in OCO-2 retrievals is demonstrated from an analysis of 2014-2019 OCO-2 XCO2raw retrievals, bias corrected XCO2bc data, ground based Total Carbon Column Observation Network (TCCON) XCO2, and Moderate Resolution Imaging Spectroradiometer (MODIS) cloud and radiance fields. In approximate
20 terms, 40 % (quality flag (QF)=0, land or ocean) and 73 % (QF=1, land or ocean) of the observations are within 4 km of clouds. 3D radiative transfer calculations indicate that 3D cloud radiative perturbations at this cloud distance, for an isolated low altitude cloud, are larger in absolute value than those due to a 1 ppm increase in CO_2. OCO-2 measurements are therefore susceptible to 3D cloud effects. Four 3D cloud metrics, based upon MODIS
25 radiance and cloud fields and stand-alone OCO-2 measurements, relate XCO2bc-TCCON averages to 3D cloud effects. This analysis indicates that the operational bias correction has a non-zero residual 3D cloud bias for both QF=0 and QF=1 data. XCO2bc –TCCON averages at small cloud distances differ from those at large cloud distances by -0.4 and -2.2 ppm for the QF=0 and QF=1 data over the ocean. Mitigation of 3D cloud biases by a
30 Table look-up technique, that utilizes nearest cloud distance (Distkm) and spatial radiance heterogeneity (CSNoiseRatio) 3D metrics, reduces QF=1 ocean and land XCO2bc – TCCON averages from -1 ppm to near ± 0.2 ppm. The ocean QF=1 XCO2bc-TCCON averages can be reduced to the 0.5 ppm level if 60 % (70 %) of the QF=1 data points are utilized, by applying Distkm (CSNoiseRatio) metrics in a data screening process. Over
35 land the QF=1 XCO2bc–TCCON averages are reduced to the 0.5 (0.8) ppm level if 65 (63) % of the data points are utilized by applying Diastkm (CSNoiseRatio) data screening. The addition of more terms to the linear regression equations used in the current bias correction processing, without data screening, however, did not introduce an appreciable improvement in the standard deviations of the XCO2bc-TCCON statistics.

1 Introduction

The Orbiting Carbon Observatory (OCO-2) measures the column-averaged atmospheric CO_2 dry air mole fraction, referred to as XCO2, on a global basis (Eldering et al., 2017).
45 Space based measurements of XCO2 can improve our understanding of surface CO_2 fluxes if XCO2 variations are accurately measured to the 0.3 % level (~1 ppm) on spatial scales

from less than 100 km over land and ~1000 km over the ocean (Rayner and O'Brien, 2001; OCO-2 L2 ATBD, 2019).

OCO-2 derives XCO2 from an optimal estimation methodology (Rodgers, 2000) that is applied (O'Dell et al., 2018) to spectra in three spectral bands: the 0.76 µm O_2 A-band, the 1.61 µm weak CO_2 band, and the 2.06 µm strong CO_2 band. The spectral resolutions of the three spectrometers are greater than 19,000 and are sufficient to resolve molecular pressure-broadened lines. Each spectral band is comprised of 1016 wavelength samples. The retrieval includes a state (solution) that includes CO_2 at 20 levels, surface pressure, H_2O and temperature profile scale factors, aerosol and cloud opacity, land or ocean surface albedo, and spectral dispersion shifts. To boost the signal to noise ratio over the dark ocean surface, XCO2 measurements over the ocean rely on sun-ocean-sensor glint viewing geometry. Measurements over land are collected in nadir or glint view geometry. A third mode, target mode, commands OCO-2 to observe many points around a specific targeted area. In this mode the sensor azimuth and zenith angles vary appreciably for a given surface location, which is not the case for the glint and nadir modes.

Clouds and aerosols definitely complicate the radiative transfer associated with the OCO-2 measurements. Connor et al. (2016) identify aerosols (solid and liquid particles) as the most important error source, followed by spectroscopic and instrument calibration uncertainties. To minimize the influence of clouds, the cloud pre-processor (Taylor et al., 2016) applies two fast algorithms to screen for clouds. The "A-band Preprocessor" solves for the surface pressure assuming that no clouds or aerosols are present. Differences greater than 25 hPa between retrieved and a priori surface pressure lead to the exclusion of a profile from the Level-2 "Full Physics" operational retrieval (OCO-2 L2 ATBD, 2019). The second algorithm compares column-integrated CO_2 from the weak and strong CO_2 bands. If the ratio of the CO_2 columns deviates significantly from unity, then the profile is excluded from the Full Physics retrieval. The preprocessors are very efficient, but they do not catch all cloudy scenes, especially if there are low altitude clouds present. Of the 1 million measurements made each day, ~25 % pass the preprocessor filters and enter the operational retrieval (O'Dell et al., 2018).

Primary validation of OCO-2 XCO2 relies upon comparison to the Total Carbon Column Network (TCCON) ground based measurements of XCO2 (Wunch et al., 2017). Twenty-seven TCCON stations (see http://tccon.caltech.edu) utilize Fourier Transform Spectrometer instrumentation. TCCON observation geometry is direct solar viewing, and the XCO2 measurements are accurate to 0.5 ppm (Wunch et al, 2010). Comparisons of XCO2raw (the XCO2 that is produced by the operational retrieval) to TCCON measurements reveal that TCCON measurements are approximately 1 ppm larger than XCO2raw values, as discussed in the Version 9 Data Product User's Guide (2018). Based upon these and other comparisons, the OCO-2 algorithm team applies multi-variable linear regressions separately over land and ocean to bias correct the XCO2raw retrievals to XCO2bc values. The variables in the bias correction equations include differences in the retrieved and a priori surface pressures, the sum of aerosol optical depths for large aerosol particles (for land data), and a "CO2graddel" term. CO2graddel is a measure of the difference in the vertical gradients of the a priori CO_2 and retrieved vertical profiles (see Eq. (5) of O'Dell et al., 2018).

Not all physics, however, is included in the Full Physics retrieval. The subject of this paper is 3D cloud effects. The operational retrieval is a 1D-column retrieval, by necessity.

The computer processing of a single profile takes several minutes. More than 100,000 profiles are retrieved per day, requiring an appreciable amount of computer processing. With regard to 3D cloud effects, radiances from a clear sky footprint may be perturbed by a cloud several kilometers from the clear sky footprint. The 1D retrieval, however, uses the independent pixel approximation, by which radiative transfer optical properties are those within a single 1D column. The 1D retrieval does not consider the radiative effects of clouds outside of the 1D column. The operational retrieval iterates for the state vector elements of the surface pressure, aerosol, surface reflectance, and the CO_2 vertical profile that minimizes the differences in the observed and forward model spectra. The state vector elements frequently take on unrealistic values in the converged solution.

Previous papers have demonstrated the presence and effects of 3D cloud effects in other experiments and the OCO-2 experiment. Várnai and Marshak (2009) demonstrated that MODIS reflectance at various wavelengths between 0.47 and 2.12 µm increases as cloud distances decrease at cloud distances less than 10 km, and that the effect is strongest at shorter wavelengths. Okata et al. (2017) modeled 3D cloud effects, finding positive 3D–1D radiance differences, for solar zenith angles greater than 5°, for periodic cuboid clouds of 2.5 km height. Merrelli et al. (2015) applied the SHDOM 3D radiative transfer code, and the OCO-2 retrieval code, and concluded that the OCO-2 cloud-screening algorithm had difficulty in rejecting clouds that filled less than half of the field of view. Retrieved XCO2 were offset low from clear sky retrievals by 0.3, 3, and 5-6 ppm for soil, vegetation, and snow surfaces. Massie et al. (2017) analyzed version 7 OCO-2 XCO2 in conjunction with MODIS radiance fields, demonstrating that XCO2 decreased as a cloud-radiance field inhomogeneity metric increased in target mode observations. Here we extend Massie et al. (2017) by analyzing additional 3D cloud metrics, and relate each of the metrics to the global set of TCCON XCO2 measurements obtained from 2014 through 2019.

Our study is organized in the following manner. In Section 2 we discuss the OCO-2, Moderate Imaging Spectroradiometer (MODIS), and TCCON data that is analyzed. Details of the bias correction procedure are presented in Section 3. We define four 3D metrics that are derived from MODIS-based files (such as nearest cloud distance) and *stand-alone* OCO-2 metrics in Section 4. We compare the utility and effectiveness of the MODIS and stand-alone metrics, since the stand-alone metrics are readily calculable from the OCO-2 data files, while the MODIS-based files impose an additional level of processing complexity. In Section 5 we demonstrate that over half of the OCO-2 measurements are within 4 km of clouds, and demonstrate in Section 6 that the 3D cloud effect over ocean and land has a larger radiative perturbation (in absolute terms) at this cloud distance than perturbations for a 1 ppm increase in XCO2. Distributions of XCO2raw –TCCON and XCO2bc – TCCON are related to the four 3D cloud metrics in Section 7. We demonstrate that 3D cloud biases in XCO2bc – TCCON remain after the current bias correction processing for both Quality Flag QF=0 (best quality) and QF=1 (lesser quality) data. While Section 7 focuses on global analyses, we demonstrate in Section 8 that the 3D effects appear readily in local scenes. Mitigation of the 3D cloud biases by application of a Table look-up correction is discussed in Section 9. Mitigation of the 3D cloud biases by data screening by the four 3D metrics is investigated in Section 10. Mitigation by adding terms to the current bias correction equations, without data screening being applied, is discussed in Section 11. Finally, Section 12 summarizes the findings of the previous sections.

2 Data

140

OCO-2 product files are available from the NASA Earthdata website (https://earthdata.nasa.gov/). Level 2 L2Std (standard) and L2Dia (diagnostic) files contain retrieved XCO2 (referred to as XCO2raw data). "Lite" files contain the XCO2raw and biased corrected XCO2bc data, with one file containing all converged retrievals for one

145 day. The Quality Flag (QF) is set to 0 for the best quality data, and to 1 for lesser quality data. Each OCO-2 measurement has an associated 16 digit Sounding ID that uniquely identifies each XCO2 profile. Over 100,000 successful retrievals are contained in a single daily Lite file. We focus upon Version 9 and 10 OCO-2 data files in our study, with the majority of presented figures and tables based upon the Version 10 data. The Version 10

150 data we analyze is derived from "beta" release files, housed at JPL, prior to the formal release to the Earthdata GES DISC archive.

Auxiliary files (Cronk et al., 2018), not archived by the NASA Earthdata file system, contain MODIS radiances at 500m spatial resolution, cloud mask, cloud fraction, cloud optical depth, and geolocation (based upon OCO-2 Version 9 data), matched to the OCO-

155 2 Sounding ID. We refer to these files as Colorado State University "CSU files". Input to these auxiliary files include MODIS 1km MYD03 geolocation, 500 m MYD02HKM radiance files, and MYD06 cloud files, which includes the 1 km MODIS cloud mask. MODIS and OCO-2 fly in formation in the NASA "A-train", with OCO-2 flying six minutes in front of MODIS Aqua. For each Sounding ID there are MODIS data points

160 within 50 km east and west of the OCO-2 observation point. In relation to each OCO-2 observation footprint, we determine the closest MODIS field point for which the MODIS cloud mask indicates a cloud, or for which the MODIS cloud optical depth is greater than unity. Knowing the geolocation positions of these two points, the distance in km between the footprint and cloud, and the angle between the observation footprint and cloud, are

165 calculated. 3D cloud effects likely are dependent upon the distance of a cloud to the observation footprint and sun-cloud-footprint viewing geometry considerations. For nadir view geometry, the OCO-2 footprint is approximately 1.3 km x 2.3 km at the Earth's surface (OCO-2 L2 ATBD, 2019). Eight adjacent footprints are arranged in a row (see Fig. 2.2 of OCO-2 L2 ATBD, 2019), and these footprints in conjunction with the observation

170 mode (ocean glint, land nadir, and target mode) determine the footprint scan patterns. Since the MODIS CSU radiances are archived at 500 m resolution, approximately 10 MODIS 500 m pixels fit within one OCO-2 footprint.

In addition to the OCO-2 and MODIS-based data, our analyses includes data files that combines this data with adjacent TCCON measurements. We refer to these files as

175 "Validation" files. A TCCON measurement is associated with an OCO-2 measurement, on the same day, if the difference in geolocation is less than 2.5° in latitude and 5° in longitude. These files allow us to calculate the statistics associated with XCO2bc-TCCON and XCO2raw-TCCON comparisons over ocean and land. Table 1 lists the TCCON sites and data used in our analyses. Wunch et al. (2015) discusses the TCOON data version we

180 analyze.

We also examine differences in averaged OCO-2 spectra, as a function of distance from nearest clouds and as a function of XCO2bc to illustrate the perturbations in radiance that are due to 3D cloud effects. OCO-2 spectra are contained in the level 2 diagnostic (glint

oco2_L2DiaGL.. and nadir oco2_L2DiaND..) files. For the spectral analysis we co-process
the diagnostic, Lite, and CSU MODIS files.

For the determination of the standard deviation of the radiances for adjacent
observation footprints, which is used to determine the H(Continuum) 3D metric discussed
in Section 4, we analyze the O_2 A-band continuum radiances that are archived in the OCO-
2 Version 10 Lev1b files (glint oco2_L1bScGL.. and nadir oco2_L1bScND..) files. The
Lev1b Version 9 files also contain "colorslice" data which is used to define the
CSNoiseRatio discussed in Section 4.

3 Bias correction procedure

As discussed by O'Dell et al. (2018) and in the Version 9 OCO-2 Data Product User's
Guide (2018, see Table 3.4), the bias correction procedure compares Level 1 retrieved
XCO2raw to TCCON XCO2, model mean XCO2, and small area analysis XCO2 and
produces *bias corrected* XCO2bc values, based upon the following equations for ocean
glint and land nadir Version 9 observations.

$$XCO2bc = (XCO2raw – Foot(fp) – Feats) / TCCONadj. \tag{1}$$

For ocean glint observations,

$$Feats = - (0.245 * dPsco2) + (0.09* (CO2graddel + 6.0)). \tag{2}$$

For land nadir observations,

$$Feats = - (0.90 * dPfrac) – (9.0*DWS) – (0.029 * (CO2graddel -15.0)). \tag{3}$$

The *footprint bias* Foot(fp) for footprints (fp) 1 through 8 varies monotonically from -0.36
to 0.34. The Version 9 TCCONadj values are 0.9954 and 0.9953 for land and ocean
observations. dPsco2 is the difference (in hPa) between the retrieved and a priori surface
pressure evaluated at the strong CO_2 band geographic location, while dPfrac (in ppm units)
is

$$dPfrac = XCO2raw * (1.00 – Papriori/ Pretrieved). \tag{4}$$

For Version 9 and 10 data the Papriori is taken from the GEOS-5 Forward Processing for
Instrument Teams (GEOS-FP-IT) analysis. CO2graddel is a measure of the difference in
the retrieved and prior CO2 vertical gradient, and is applied in Eq. (2) if CO2graddel is less
than -6.0. DWS is the sum of the vertical optical depths of the dust, water, and seasalt
aerosol components.

As discussed by O'Dell et al. (2018), the small area analysis XCO2 is based upon the
assumption that XCO2 should be uniform in a 100 km by 100 km region, since the XCO2
decorrelation length is between 500 and 1000 km. The model median data is taken from an
ensemble of six models. The Feats coefficients are determined from a comparison of Feats
coefficients derived separately from comparisons of XCO2raw with TCCON XCO2,
model mean XCO2, and small area analysis XCO2. The TCCONadj divisor is based solely

230   on TCCON data. In this paper we focus solely upon analysis of XCO2 –TCCON data since the TCCON data is the most direct truth proxy of the three proxies.

       For Version 10 data Eq. (2) still applies, but with dPsco2 and CO2graddel coefficients of 0.213 and 0.0870, and TCCONadj equal to 0.995 (Version 10 OCO-2 Data Product User's Guide (2020), see Table 3.3). For land observations,

235

$$Feats = \ -(0.855 * dPfrac) \ - \ 0.335 * (max(logDWS,-5) + 5.0)$$
$$-(0.0335 * (CO2graddel\ -5.0)) \ + \ 5.20\ (AODfine\ -0.03), \qquad (5)$$

    where AODfine is the fine aerosol optical depth (sulfate plus organic carbon aerosol), and
240   TCCONadj is equal to 0.9959. The Version 10 and 9 Foot(fp) values differ slightly.

       In the application of Eqns. (1) – (3), the retrieval provides dPsco2, dPfrac, DWS, and CO2graddel bias correction values that are used in the bias correction calculations. The XCO2raw values are designated as QF=0 or QF=1 data points from a series of exceedance checks on many variables, including the bias correction variables. The operational bias
245   correction only uses the QF=0 data points to determine the linear coefficients in Eqns. (2) and (3).

       The differences in XCO2raw and XCO2bc are due to several factors. First of all, there are uncertainties in the spectroscopic parameters (line strengths, pressure broadening coefficients, energy levels, and specifications of the molecular line shape, including line-
250   mixing complications). Calibration errors, especially in regard to the instrument line shape, are also important. Incorrectly modeled physical scene characteristics, such as errors in the aerosol single scattering property or surface bidirectional diffuse reflectance (BRDF) specification, and/or 3D cloud scattering considerations, also have influence upon the XCO2raw and XCO2bc differences.
255   The operational retrieval, however, does not include 3D cloud effects. We will calculate 3D cloud metrics based upon the MODIS files and "stand alone" OCO-2 data, and investigate if application of the 3D metrics in a Table look-up correction, or by data screening by the 3D metrics, leads to a reduction in the standard deviations and averages of TCCON-XCO2bc probability distribution functions (PDFs). We also add 3D cloud
260   metric terms to the bias correction Eqns. (1)-(3) to determine if they reduce TCCON-XCO2bc standard deviations and averages.

4 Metrics

265   Several 3D metrics are calculated from MODIS and OCO-2 data files. Nearest cloud distance (abbreviated as Distkm), the sun-cloud-footprint scattering angle, and the H(3D) metrics (discussed below) are calculated from MODIS data files. The CSNoiseRatio and the H(Continuum) metrics (discussed below) are calculated from *stand-alone* OCO-2 data. We will apply all of the metrics in subsequent sections of this paper, and compare how well
270   each metric performs in reducing the scatter in the TCCON-XCO2bc standard deviations and averages over ocean and land.

       The CSU files are processed to determine the distance in km of the OCO-2 Lite file observation data points to the nearest MODIS cloud. The distance is simply the hypotenuse of the triangle formed by the difference in latitude and longitude of the center of the OCO-
275   2 footprint and the nearest MODIS cloud, with the longitude difference multiplied by the

cosine of the latitude. The sun-cloud-footprint scattering angle is the angle between the sun to nearest cloud vector and the nearest cloud to observation footprint vector. The Distkm metric frequently refers to clouds that are *outside* of the geospatial scan pattern defined by the OCO-2 observation footprints. A representative scan pattern is illustrated in Fig. 9, for glint (ocean) scene. There are clouds within and outside of the geospatial scan pattern of the footprints marked by the asterisks. If a cloud is inside a footprint, then the cloud would add photons to the sensed radiance, and any cloud shadows would provide lesser sensed radiance. The Distkm metric cannot be specified from OCO-2 observations.

The H(3D) metric (Liang, Di Girolamo, and Platnick, 2009; Massie et al., 2017), as applied to the radiance field,

$$H(3D, kcir) = \text{standard deviation of the Radiance field / average of Radiance field,} \quad (6)$$

is a measure of the *inhomogeneity* of the radiance field, and is calculated from the CSU file radiance fields. For a cloudless scene with no surface reflectance variations, the H(3D) parameter approaches zero, while for scenes with broken cloud fields or surface reflectance heterogeneity, the H(3D) metric is larger. The H(3D, kcir) values are calculated for four averaging circle radii (kcir) of 5, 10, 15 and 20 km, that surround each OCO-2 footprint. 95 % of the H(3D) values vary between 0.0 and 0.80 over the ocean and between 0.0 and 0.66 over land. The 10 km circle H(3D) data is used in our study. Fig. 1 of Várnai and Marshak (2009) indicates that MODIS reflectance at wavelengths between 0.47 and 2.12 μm increased (i.e. that 3D cloud effects are present) for cloud distances less than 10 km, with nearly zero increase in reflectance at larger distances. We find that there is a larger inhomogeneity in the radiance field over the ocean than over the land. The H(3D) metric increases as cloud inhomogeneity increases.

The OCO-2 CSNoiseRatio uses the sub-footprint spatial information contained within the "colorslice" data. As discussed by Crisp et al. (2017, see their Fig. 2), each of the 8 footprint samples are an average of 20 pixels. For a subset of 20 columns (the spectral dimension), the individual pixel level data is returned from the instrument and stored as "colorslices" in the level 1 L1b data files. The specific 20 columns are chosen at specific spectral locations in each of the OCO-2 bands, primarily to support the de-clocking algorithm. Each band contains 5 or 6 colorslices at continuum wavelengths. The spatial mean and standard deviation are computed for each of these continuum colorslices, and then the final mean and standard deviation for that individual sounding is computed across those 5 to 6 values. Computing a median over the available continuum slices makes the calculation robust to isolated bad pixel values, which can be caused by cosmic ray hits on the detectors. The "CSNoiseRatio" used in this paper is the ratio of the continuum radiance spatial standard deviation and the noise level at the continuum radiance level as predicted from the radiometric noise model. The CSNoiseRatio has an expected value of unity if the continuum radiance in the footprint is spatially constant, as the standard deviation across the pixels should be due to the detector noise. The CSNoiseRatio values increase as the within-footprint radiance inhomogeneity increases. Note that each observation footprint has an extent of approximately 1.3 km (cross-track) by 2.3 km (along-track) at the Earth's surface. The CSNoiseRatio values increase as cloud inhomogeneity, within and/or outside of each observation footprint, increases.

Finally, the H(Continuum) metric is calculated from Eq. (7), based upon the observed radiance Radobs at a specific footprint, and the standard deviation of the radiance field, with radiances given by the OCO-2 O_2 A-band level1b *continuum radiances*.

325   H(Continuum) = 100 (standard deviation of the Radiance field / Radobs),   (7)

For a specific observation footprint, we focus upon the primary west to east row of eight adjacent footprints that contains the specific footprint, and two adjacent rows, one north and one south of the primary row (see Fig. 9, discussed below). There are therefore 23
330   adjacent footprints that we associate with a specific footprint. For each specific footprint, the 23 adjacent footprint continuum radiances are included in each H(Continuum) calculation. All footprints are given equal weight in applying Eq. (7), including footprints 1 and 8 (the edge footprints). 95 % of the O_2 A-band H(Continuum) values vary between 0 and 24 over the ocean, and between 0 and 27 over land. H(Continuum) increases as cloud
335   inhomogeneity increases.

    Of the four metrics, the nearest cloud metric is directly tied physically to the cloud field of a given scene, and is assessed over a wide spatial scale. The radiance inhomogeneity (radiance standard deviation) based metrics are indirectly tied to the cloud field, with the CSNoiseRatio and H(Continuum) metrics assessed over a lesser spatial range. We note,
340   however, that a cloud field usually has more than one cloud, so the nearest cloud metric incompletely describes the cloud field.

5 The proximity of OCO-2 observations to clouds

345   Figure 1 presents the fraction of Lite file glint and nadir observations that have a cloud within a circle of a specified radius in km, in summer for five 20º latitude bands, for 2014 - 2019. The calculations utilize distance bins from 0 to 35 km, with fractions normalized to 100 % for the 35 km circle radius. In approximate terms, 40 % (QF=0, glint or nadir) and 73 % (QF=1, glint or nadir) of the observations are within 4 km of clouds. The tropical
350   0º-20º and -20º-0º latitude bands have observations that are closest to clouds. This is of importance since the tropics have relatively few OCO-2 observations, compared to other latitudinal bands. Carbon cycle fluxes in the tropics are large and are very important in regards to understanding the global carbon cycle.

    Table 2 presents the fraction of observations that have a cloud within 4 km of an
355   observation for each season. The minimum and maximum values for the four seasons are in the 21-58 % and 55-96 % ranges for the QF=0 and QF=1 cases. Averaged over the year, 40 % and 75 % of the QF=0 and QF=1 observations are within 4 km of a cloud. Fig. 1 and Table 2 indicate that OCO-2 QF=1 data is appreciably closer to clouds than the QF=0 data. The QF=1 data is therefore more susceptible to 3D cloud effects than the QF=0 data.
360

6 Radiative Transfer Sensitivity Calculations

    To illustrate the relative sensitivity of glint and nadir observations to 3D cloud effects, we applied the Spherical Harmonic Discrete Ordinate radiative transfer Method (SHDOM) 3D
365   radiative transfer code to the same sparse cloud scene, varying glint and nadir viewing geometry and other parameters (surface reflectance). This cloud scene is illustrated below

in Fig. 9. SHDOM (Evans, 1998; Pincus and Evans, 2009) is applied by specifying a 3D model atmosphere with a specified 3D field of cloud optical properties. Radiation fields at satellite altitude for 1D column (independent pixel approximation, IPA) and 3D mode are
370 calculated separately. Comparison of the IPA and 3D calculations then indicates the size of the 3D cloud effect radiative perturbations.

Figure 2 presents SHDOM radiative perturbations for all three OCO-2 bands, based upon the atmospheric base-state and perturbed parameters given in Table 3, with monochromatic total optical depth at representative wavelengths on the x axis and radiative
375 perturbations on the y axis. Perturbations are applied individually one at a time, e.g. for the calculation of the partial derivative of radiance with respect to a change in surface pressure, all other variables are kept at their base state values. The base state CO_2 is 400 ppm at a surface pressure of 1016 hPa.

The cloud field is derived from the MODIS 250 m radiance field on June 12, 2016 over
380 the ocean (and graphed in Fig. 9). As discussed by Massie et al. (2017), the MODIS cloud mask does not identify all clouds that are visible in MODIS imagery (available from the NASA Worldview website https://worldview.earthdata.nasa.gov/). MODIS 250 m field radiance and MODIS cloud mask data can be used together to generate a cloud field that includes cloud elements not identified by the MODIS cloud mask. The SHDOM cloud field
385 assigns a cloud to a location if the MODIS radiance at that location is greater than or equal to scene-specific MODIS radiance thresholds. The scene-specific radiance thresholds are calculated from the radiances at scene locations in which the cloud mask indicates a cloud, and/or when the MODIS cloud optical depth is greater than unity. The cloud height is set at 1.8 km. This is the median height of the PDF of trade wind cumuli heights determined
390 from an analyses of 30m Advanced Spaceborne Thermal Emission and Reflection (ASTER) stereo data (Genkova et al. 2017). This is also the cloud height used by Massie et al. (2017) in their 3D calculations for an OCO-2 target mode observation centered over the Lamont, Kansas TCCON site.

A separate computer program calculates the three dimensional distribution of water
395 droplets and aerosol particles in the x-y-z grid, writing to an offline data file. This file specifies the liquid water contents and effective radii of the water droplets, and the aerosol mass densities and effective radii. We specified water droplets to have an effective radius of 10 μm, and aerosol particles an effective radius of 0.1 μm. SHDOM uses a Mie calculation to write to a particle scattering table for a range of water droplet effective radii
400 (for a gamma size distribution), and a similar table for the aerosol particles (for a lognormal size distribution). These two tables, and the offline input file, are used by SHDOM to specify the particle absorption, scattering, and phase function particle characteristics in the x-y-z grid.

The 1D calculations are perturbed (see Table 3) individually by 10 hPa and 10 ppm for
405 surface pressure and CO_2 perturbations, and by surface reflectance (for nadir) or surface wind (for glint), and aerosol optical depth perturbations. Aerosol optical depth vertical structure is the same for all x-y grid points, but the total aerosol optical depths are equal to e.g. 0.11 and 0.165 for the base and perturbed state O_2 A-band calculations The OCO-2 ABSCO database of molecular line cross sections (Payne, 2016) is used to specify the gas
410 optical depth structure in the x, y, z 3D grid (of size 32 km x 32 km x 30 km, with a horizontal grid cell size of 0.5 km x 0.5 km). SHDOM was applied in monochromatic calculations at 17 wavelengths, in which the total gas plus aerosol optical depth ranges

from small to large values, for Lambertian surface scattering over land and Cox-Munk surface wind dependent bidirectional diffuse reflectance over the ocean.

415   The curves labeled as "3D" in Fig. 2 are percent differences between the 3D and 1D calculations, for base state conditions, at an observation footprint 4 km west of a typical cloud in the MODIS cloud field (with the sun along the negative x axis at a solar zenith angle of 20°). Shadows are not located at this observation footprint since the sun and footprint are to the west of the cloud. The other curves are 1D perturbations, normalized to

420   the stated perturbation amount. For example, the "1 ppm CO2" curve is derived by dividing the SHDOM radiance field differences for the 400 and 410 ppm conditions by 10. The 1D curves are radiance perturbations also at 4 km from the cloud, and since the 1D column calculation does not have any knowledge of nearby clouds, the 1D curves are not influenced by nearby clouds. All of the panels in Fig. 2 have x-axes expressed in terms of

425   the gas plus aerosol vertical optical depths of the base state atmosphere. 3D radiative perturbations are largest at small optical depths, while 1 ppm CO_2 perturbations are largest at large optical depths. This indicates that 3D cloud effects impose spectral perturbations with an optical depth structure that differs from CO_2 mixing ratio perturbations.

Figure 2 indicates that a cloud 4 km away from a clear sky footprint has 3D cloud effect

430   radiative perturbations in the WCO2 and SCO2 bands that are larger at small optical depths than a 1 ppm CO_2 perturbation. The WCO2 (SCO2) perturbations are near 2.1 % (1.5 %) and 1.4 % (1.0 %) for the glint and nadir cases, while the "1 ppm CO2" curves have values less than 1 % in absolute value. This comparison is relevant since the observational goal of OCO-2 is to measure XCO2 to 1 ppm accuracy on regional scales. OCO-2 observations

435   therefore are susceptible to 3D cloud effects.

From a radiative transfer perspective, Fig. 2 indicates that ocean glint observations are more susceptible to 3D cloud effects than land nadir observations. Since Fig. 1 and Table 2 indicates that clouds are closer to observations over the ocean than over land, the Fig. 1 and 2 calculations, in combination, indicate that 3D cloud effects are likely more prevalent

440   for the ocean glint measurements.

The Fig. 2 calculations are not influenced by cloud shadows, since the observation point is west of the cloud position. While Fig. 2 focuses upon radiative perturbations away from a cloud, 3D cloud effects also include cloud shadows, which decrease the sensed radiances. It is expected that radiance enhancements and radiance dimming both occur in OCO-2

445   observations, which can yield both negative and positive XCO2 variations to the local scene.

It is expected that viewing and scattering geometry play an important role in 3D cloud effects. Liquid and ice particles have phase functions which have dominant forward scattering peaks, and the scattering of solar photons off of the side of a cloud is an important

450   component of the 3D cloud effect. Fig. 3 illustrates the angular dependence of 3D cloud effects along a circle of 4 km radius that surrounds an isolated cloud. The calculations refer to a continuum wavelength with the smallest possible gas optical depth. Observation footprints are to the west, north, east, and south of the cloud at angles of 0º, 90º, 180º, and 270º, with the sun at the 0° angle along the negative x-axis and the sensor along the positive

455   x-axis. There is a factor of two variation, as a function of the location of the observation footprint, in the 100 (3D-IPA) / IPA values. The largest values occur when the observation footprint is west of the cloud (angle=0°). The solar beam scatters off of the west side of the cloud back to the observation footprint, which is followed by additional scattering off of

the surface towards the sensor along the positive x axis. This solar beam side-of-cloud scattering contribution does not take place when the observation footprint is east of the cloud (angle=180°), so the 3D effect is then smaller.

Since the OCO-2 cloud screening preprocessor frequently does not reject scenes with a few low altitude "popcorn" clouds, the metrics of nearest cloud distance and the sun-cloud-observation footprint scattering angle are useful rudimentary metrics to characterize a cloud scene. But they do not characterize completely a cloudy scene with numerous clouds. As more and more clouds are added to a scene that surrounds an observation point, there is a complicated interaction of perturbative effects from the individual clouds

7 Global statistics

The Validation files reveal the dependencies of XCO2bc-TCCON and XCO2raw-TCCON upon the various 3D metrics. Fig. 4 presents contour maps of the number of XCO2raw-TCCON and XCO2bc-TCCON observations over the ocean versus nearest cloud distance. There are more data points at smaller than at larger cloud distances, especially for the QF=1 data. The bias correction moves the center of the XCO2raw-TCCON distributions upwards towards the XCO2bc-TCCON = 0 line, especially for the QF=0 data. This is not as apparent for the QF=1 distributions, keeping in mind that QF=1 data is not used in the operational bias correction calculations. For the 0 to 2 km cloud range there is a noticeable asymmetry in the QF=1 distributions, with a "tail" of negative XCO2bc-TCCON data points. This is visually apparent by following the aqua-marine-blue contour line from larger to smaller cloud distance.

Figure 5 presents contour maps of counts of XCO2raw-TCCON and XCO2bc-TCCON over the ocean versus the CSNoiseRatio metric. As mentioned above, the CSNoiseRatio values increase as the radiance field inhomogeneity (and cloudiness) increases. The QF=0 data has most of the CSNoiseRatio values near unity, consistent with spatially uniform radiance conditions. A wider range of CSNoiseRatio values is seen in the QF=1 data, indicating relatively more observations impacted by spatially variable radiance. The H(3D) and H(Continuum) variables have contour maps similar in visual appearance to the Fig. 5 CSNoiseRatio contour map.

Table 4 presents the minimum standard deviations in the data displayed in Fig. 4 and 5, and the range in the ratios of the standard deviations. Standard deviations in XCO2-TCCON are calculated as a function of Distkm in bins of 2 km cloud distance for both XCO2raw and XCO2bc. The minimum standard deviation is the smallest of the set of standard deviations. The range of the standard deviations is the ratio of the largest to smallest standard deviation in the set of standard deviations. As an example, the ocean QF=0 minimum standard deviations are 1.04 and 0.76 ppm for XCO2raw and XCO2bc in Fig. 4 for the Distkm metric, while the ratios of maximum to minimum standard deviations are 1.16 and 1.26 for the XCO2raw and XCO2bc data. Table 4 also presents the minimum and standard deviation ratios for the H(3D), CSNoiseRatio, and H(Continuum) metrics. Generally, the minimum standard deviations are larger for the QF=1 case, the biased corrected standard deviations are less than the raw retrieval standard deviations, the ratios deviate from unity, and all metrics display these characteristics. If the OCO-2 retrievals were not susceptible to 3D cloud effects, then the ratios in the lower half of Table 4 would be close to unity, but this is not the case.

505   Further insight into the Fig. 4 and 5 distributions is presented in Fig. 6 and 7, in which averages and 95 % (2σ) confidence limits of the averages are displayed. The XCO2raw-TCCON and XCO2bc-TCCON averages become more negative for both QF=0 and QF=1 cases as cloud distance approaches zero in Fig. 6. The averages become closer to each other as nearest cloud distance increases to large values. Ideally, the XCO2bc-TCCON

510 differences should approach zero as the nearest cloud distance becomes very large, since the 3D effect should physically decrease towards zero as cloud distance becomes very large. The differences are close to 0.4 ppm in Fig. 6 instead of zero since the operational bias correction processing also considers comparisons of XCO2raw and model XCO2 in the determination of XCO2bc (O'Dell et al. 2018). Since the 95 % confidence limits in Fig.

515 6 do not overlap for small cloud distances, the differences in the averages, and the increasingly negative trend in the averages as cloud distance approaches zero, are statistically significant. This indicates that the operational bias correction does not completely remove 3D cloud effects from the XCO2raw retrievals for the full range of cloud distance. Fig. 6 indicates that there is a difference in the XCO2bc – TCCON averages

520 near -0.4 ppm (the difference of 0 ppm at cloud distances near 0 km and 0.4 ppm at cloud distances greater than 10 km). This difference is referred to as the ocean 3D *cloud bias*.

   For ocean QF=1 XCO2bc the 3D cloud bias is -2.2 ppm. Since 40 % (75 %) of the QF=0 (QF=1) data points observations over the ocean are within 4 km of clouds, it is apparent that many OCO-2 data points are subject to a negative 3D cloud bias that is not

525 completely removed by the operational bias correction. The corresponding 3D cloud biases for XCO2bc-TCCON over the ocean for QF=0 and QF=1 data (for the CSNoiseRatio metric) are -1.3 and -1.4 ppm (see Fig. 7). The -1.4 ppm values is equal to the difference of -1.8 ppm (at the CSNoiseRatio of 7) minus -0.4 (at the CSNoiseRatio of 1). As mentioned above, radiance field inhomogeneity increases as the CSNoiseRatio increases.

530 The XCO2bc-TCCON cloud biases for the QF=1 data for the Distkm and CSNoiseRatio variables, -2.2 and -1.4 ppm, differ somewhat in absolute size, but are consistent in sign (both are substantially negative).

   The data presented in Fig. 6 and elsewhere in this paper could also be influenced by the presence of undetected cloud fragments, dissipating clouds, and the fact that relative

535 humidity is enhanced directly outside a cloud. The increase in relative humidity leads to swelling of aerosols, which would enhance near-cloud aerosol scattering. Twohy et al. (2009) measured relative humidity and aerosol scattering in the vicinity of small marine cumulus during the 1999 Indian Ocean Experiment (INDOEX). Enhancements were observed within 1 km of the cloud. Observations and model simulations of "cloud haloes"

540 by Lu et al. (2002) and Lu et al. (2003) also indicate that the cloud haloe exists ~ ½ km from a cloud. From Fig. 6, however, the XCO2bc-TCCON averages asymptote to a constant value over a length scale of 10 km, a scale substantially larger than the 1 km scale associated with cloud haloes. This disfavors an interpretation that the variation in Fig. 6 is primarily due to cloud haloe effects. Várnai and Marshak (2009) also concluded that

545 aerosol swelling does not account for observed illuminated / shadowy asymmetries in MODIS shortwave reflectance versus nearest cloud distance data.

   Table 5 summarizes the 3D cloud biases derived from the four 3D metrics. In general, the cloud biases are all negative for the Distkm, CSNoiseRatio, and H(Continuum) 3D metrics over the ocean for the QF=0 data. The graph of the QF=1 XCO2bc-TCCON

550 averages as a function of the H(3D) metric has a minimum at H(3D) near 0.9, maxima at

H(3D) near 0.1 and 1.3, and a range of XCO2bc-TCCON averages that span 1.6 ppm. Table 5 indicates this non-linear (quadratic) curve characteristic with the ± symbol. Since the bias correction equations in Section 3 are based upon linear equations, the extension of these equations with linear H(3D) metric terms (see Section 11) is expected to be of limited utility.

The Table 5 cloud biases for V9 and V10 data are fairly close to each other. As an example, the V9 and V10 cloud biases for the cloud distance variable are -2.5 and -2.2 ppm for QF=1 ocean data. These similarities indicate that 3D cloud effects persist irrespective of data version.

It is instructive to examine graphs of x=cloud distance versus y=dPsco2 (over the ocean) and x=cloud distance versus y=dPfrac (over land). Fig. 8 presents the averages and the 95 % confidence limits of the averages. dPsco2 is fairly constant for large cloud distances for QF=0 data, then becomes increasingly negative as cloud distance approaches zero. The range of dPsco2 is -0.6 and -3.6 hPa for the QF=0 and QF=1 ocean data, and the range of dPfrac is -0.3 and -2.2 ppm for the QF=0 and QF=1 land data. With 40 % and 75 % of the observations at distances less than 4 km for QF=0 and QF=1 data, the dependence of x=cloud distance and y= dPsco2 in Fig. 8 can be described by a linear line with positive slope (and less so for the y=dPfrac land data). Since dPsco2 and dPfrac are included in the operational bias correction (Eqns. (1) through (5) of Section 3), and these metrics are correlated to the cloud distance metric, the operational bias correction *indirectly* "takes into account" 3D cloud effects.

8 Illustrative ocean scenes

While the previous section discussed global analyses, it is important to point out that 3D cloud biases are readily apparent at local scales. Fig. 9 displays glint data over the Pacific on June 12, 2016. MODIS clouds are indicated by irregular red shapes, while OCO-2 observations are indicated by color coded asterisks. For each horizontal row of asterisks there are eight adjacent OCO-2 footprints. Nearest cloud distance is indicated in the top panel, and H(Continuum) values are indicated in the middle panel. The H(Continuum) values increase in size for the region surrounding the cloud at 15.6° N, with blue asterisks (low H(Continuum)) morphing into red and green asterisks (high H(Continuum)) as cloud distance decreases. In the bottom panel the Quality Flag becomes QF=1 for data points adjacent to this cloud feature.

The upper panel of Fig. 10 presents XCO2bc versus nearest cloud distance from data on June 12, 2016 for the 11° N – 17 °N, 158 ° E – 177° E range of latitude and longitude, which is larger than the Fig. 9 geospatial range. Only XCO2bc is graphed in Fig. 10 since TCCON data is not available for this ocean scene. At largest cloud distances the QF=1 XCO2bc data points span a limited range of XCO2bc, from 403 to 406 ppm. For the 0 to 2 km cloud distance range, the XCO2bc data points vary from 398 to 410 ppm, with a noticeable "negative tail" of XCO2bc less than 403 ppm. Ranges of XCO2bc are binned into High, Mid, and Low bins of XCO2bc.

The bottom panel of Fig. 10 presents average O_2 A-band spectra for the spectra associated with the three XCO2bc bins. The bottom panel indicates that 3D cloud effects perturb the "Mid" radiances in the O_2 A-band by ± 15 % in this glint scene. In a comparative manner, the radiance perturbations for the O_2 A-band, WCO2, and SCO2 bands are ± (6,

7, 7) % and ± (15, 15, 18) % for the QF=0 and QF=1 cases. 3D cloud effect radiance perturbations are therefore large for all three bands.

The operational retrieval iteratively solves for a state vector (which includes surface pressure, aerosol, surface reflectance, the CO_2 vertical profile, and other variables) that matches observed and forward model radiances. Since 3D cloud radiative perturbations are not incorporated into the operational retrieval, the retrieved surface pressure, aerosol, surface reflectance, and CO_2 vertical profile, will differ from the actual atmospheric values. These differences will increase as the severity of the 3D cloud effect increases at small cloud distances. Since 3D cloud effects perturb all bands, the retrieved surface pressure differs from the actual surface pressure, and this difference propagates into the XCO2raw retrieval.

For a range of latitude (52° S - 41°S) and longitude (164° E - 180° E), with Lauder, New Zealand being the closest TCCON site, Fig. 11 displays scatter diagrams of TCCON – XCO2bc, CSNoiseRatio, dPsco2, CO2graddel, DWS, and O_2 A-band surface reflectance, as a function of cloud distance. All observations during 2017, for which TCCON data is matched to the OCO-2 observations, are considered, with most of the data points observed during November and February. The QF=0 and QF=1 data points in Fig. 11 are color coded by green and red symbols, respectively. The various panels consistently indicate that dPsco2 and CO2graddel values are near zero for QF=0 data points, and are accompanied by low DWS, surface reflectance, and CSNoiseRatio values, for both small and large cloud distances. The measured QF=1 CSNoiseRatio becomes progressively larger as cloud distance decreases. For QF=1 data the dPsco2, CO2graddel, DWS, and surface reflectance variables take on unrealistic values as cloud distance decreases from large to small values.. These unrealistic values are necessary in order for the retrieval to match observed and forward model radiances. When the 3D cloud effect adds radiance to the observations, a large DWS or reflectance value is able to increase the forward model radiance to the measured radiance.

9 XCO2 Cloud Bias Mitigation by Table look-up correction factors

Figures 6 and 7 suggest mitigation of 3D cloud biases by application of a Table look-up correction. Using the CSNoiseRatio QF=1 data as an example, and the XCO2raw data points, for a given XCO2raw data point there is a corresponding CSNoiseRatio value and XCO2raw-TCCON average (see the upper right panel in Fig. 7). The corrected XCO2raw value (XCO2raw,corr) is then simply the XCO2raw value *minus* the XCO2raw-TCCON average. The lower right panel of Fig. 7 can be used in a similar calculation to specify QF=1 XCO2bc,corr values. Note that these Table look-up table mitigation calculations can be applied after the operational bias-correction processing, with XCO2raw,corr and XCO2bc,corr data added to the data included in Lite files, provided that the CSNoiseRatio and/or Distkm values that correspond to the OCO-2 observations are known.

Table 6 presents statistics of Table look-up cloud bias mitigation calculations, corresponding to calculations in which the four 3D metrics are applied separately to the raw and bc data. The two "Standard" rows in Table 6 refer to standard deviations and PDF averages of XCO2bc-TCCON, based upon Lite file XCO2bc. The rest of Table 6 then presents the statistics (PDF averages and standard deviations of XCO2raw,corr-TCCON

and XCO2bc,corr - TCCON) of the ocean and land QF=0 and QF=1 corrected data, for the four 3D metrics.

Table 6 indicates that the Table look-up technique changes XCO2-TCCON averages, but not their standard deviations. The XCO2bc,corr-TCCON standard deviations for QF=0 and QF=1 data over land and ocean are close to the standard deviations of the "Standard" values. The "Standard" XCO2bc-TCCON averages for QF=1 ocean and land data are near -1 ppm, while the corrected XCO2bc,corr data has PDF averages near or less than 0.2 ppm, depending upon which 3D metric (and its associated set of XCO2bc-TCCON averages) is applied. Since the XCO2bc-TCCON "Standard" averages are already small (0.3 ppm and 0.11 for QF=0 data over ocean and land), the Table look-up mitigation technique is therefore more beneficial for the QF=1 XCO2bc data than for the QF=0 XCO2bc data.

The data in Table 6, however, does not reveal a shortcoming of the Table look-up mitigation technique, when only a *single* 3D metric is applied. Using the CSNoiseRatio 3D metric as an example, the use of the Fig. 7 CSNoiseRatio averages yields a corrected set of XCO2bc,corr values and new XCO2bc,corr – TCCON averages (in a revised Fig. 7 graph, not shown) in which the new averages are very close to zero, binned as a function of CSNoiseRatio. The corresponding revised Fig. 6, based upon the CSNoiseRatio correction, however, displays a large range of XCO2bc,corr – TCCON averages when the averages are binned as a function of Distkm.

The general situation is indicated in Fig. 12. The x and y axes are bins of Distkm and CSNoiseRatio, with contouring of XCO2raw – TCCON and XCO2bc – TCCON from -5 to 1 ppm. In the construction of Fig. 12, the adopted Distkm and CSNoiseRatio set of bins had a finer (coarser) bin increment for small (large) values of Distkm and CSNoiseRatio, in order to include a similar number of data points for each x-y grid cell. In Fig. 12 the largest variation in XCO2raw – TCCON and XCO2bc – TCCON is present along the Distkm axis, especially for the QF=1 data, while the variation is smaller along the CSNoiseRatio axis (e.g. for small Distkm values). Though the Table 6 CSNoiseRatio "bc ave" value of XCO2bc,corr – TCCON for QF=0 (QF=1) ocean data is near 0.06 (0.09) ppm, the revised Fig. 6 graph indicates that the XCO2bc,corr – TCCON averages vary by 0.3 (-1.9) ppm as a function of the Distkm metric. The mitigation of the cloud bias by the CSNoiseRatio 3D metric therefore does not remove the 3D cloud bias when one examines the 3D cloud bias in a XCO2bc,corr – TCCON versus Distkm graph.

Using the Fig. 12 data as the basis for a Table look-up correction, new Fig. 6 and 7 averages are displayed in Fig. 13 and 14, and were calculated as follows. For a given pair of Distkm and CSNoiseRatio values that are associated with a single XCO2 measurement, the Fig. 12 XCO2raw – TCCON or XCO2bc – TCCON values for the specific Distkm, CSNoiseRatio pair is subtracted from the XCO2raw and XCO2bc values. Applying the Fig. 12 corrections to all of the XCO2 measurements, Fig. 13 and 14 indicate that the revised XCO2raw,corr – TCCON and XCO2bc,corr – TCCON averages are then within ± 0.2 ppm of zero for both 3D metrics. Figures (not shown) for the corresponding corrected averages over land are also within ± 0.2 ppm of zero, with the exception of one data point. The utilization of the Fig. 12 data, in which both Distkm and CSNoiseRatio 3D metrics are used in a Table look-up application, appears to be a better way to mitigate for 3D cloud biases compared to single-variable Table look-up calculations.

An additional calculation was carried out in which the Fig. 12 data was fit by linear regression, represented by a constant term plus Distkm and CSNoiseRatio terms. Four x-y

fits were calculated, one for each of the four panels in Fig. 12. This representation was then applied as the basis for correction of the XCO2 data. This calculation yielded Fig. 13 and 14 style graphs which had *larger ranges* in the XCO2raw,corr – TCCON and XCO2bc,corr – TCCON averages than those based upon the Fig 12. Table look-up technique.

Figure 12 therefore has variations which are not easy to represent by a linear regression. This has bearing upon the calculations discussed below in Section 11 in which 3D metrics are added to the operational bias correction equations. The comparison here of the two calculations, based upon the Table look-up and x-y linear regression representations of the Fig. 12 data, suggests that the Table look-up technique is a better 3D cloud bias mitigation technique.

10 Mitigation by data screening

Another way to mitigate for 3D cloud biases is to apply 3D metric *data screening*. Table 7 presents standard deviations and PDF averages of XCO2bc-TCCON over the ocean for various data screening thresholds, and is read in the following manner. Referring to Distkm as the nearest cloud distance, ocean QF=0 XCO2bc-TCCON data for Distkm between 2 and 50 km has a standard deviation of 0.80 ppm, with a sample size fraction of 0.83 of the total possible number of QF=0 data points, and the average of the XCO2bc-TCCON PDF is 0.36 ppm. For Distkm between 5 and 50 km, the standard deviation is 0.78, with a sample fraction of 0.62 of the QF=0 data points, and the PDF average is 0.40 ppm. For QF=1 data the standard deviations for these two Distkm screening thresholds are 2.03 and 1.89 ppm, with sample fractions of 0.41 and 0.19, with PDF averages of -0.16 to 0.36 ppm.

Table 7 indicates that the PDF averages are already acceptable for QF=0 ocean data, since PDF averages (in absolute value) are less than 0.5 ppm (a reasonable mitigation goal) when no screening is done. For QF=1 ocean data, however, the standard deviations and PDF averages change substantially as the cloud distance threshold screening is applied. If all data points are accepted, then the standard deviation is near 2.3 ppm, and the XCO2bc-TCCON PDF average is near -0.99 ppm. For a cloud distance threshold near 1 km the data screening reduces the average of the XCO2bc – TCCON PDF to near 0.5 ppm (in absolute value), with a sample fraction near 0.60.

H(3D), CSNoiseRatio, and H(Continuum) screening thresholds, and their associated standard deviations and XCO2bc-TCCON PDF averages over the ocean are also summarized in Table 7. For the QF=0 data the data screening changes the deviations and averages by very small amounts. For the QF=1 data the data screening yields substantial changes in the deviations and PDF averages. The H(3D), H(Continuum), and CSNoiseRatio, screening thresholds of 0.57, 14, and 4.2 yield XCO2bc-TCCON PDF averages (in absolute value) near 0.5 ppm, with sample fractions of 0.72, 0.73, and 0.70. We note that the H(Continuum) and CSNoiseRatio metrics, however, are from *stand-alone* OCO-2 measurements, while the nearest cloud distance and H(3D) metrics rely upon MODIS measurements.

Table 8 indicates that the PDF averages are already acceptable for QF=0 land data, since PDF averages (in absolute value) are less than 0.5 ppm when no screening is done For QF=0 data, with no data screening, the standard deviations over land (near 1.2) are larger than those over the ocean (near 0.8, see Table 7). For QF=1 data, the changes are substantial, with deviations changing from 4 to 2 ppm for the Distkm screening, and from

3.6 to 2.8 ppm for the other metrics. The PDF averages decrease to the 0.5 ppm level (in absolute value) when approximately 0.65 of the Distkm data points are utilized, by only using data with nearest cloud distances greater than 2.2 km. While the CSNoiseRatio metrics do not decrease the XCO2bc-TCCON deviations and PDF averages to the 0.50 ppm level (see column 12 of Table 8), the PDF averages decrease to the 0.8 ppm level (in absolute value) when approximately 0.63 of the CSNoiseRatio data points are utilized, by only using data with CSNoiseRatio values less than 3.4.

Figure 15 displays the changes in the PDFs over the ocean and land as a function of nearest cloud distance screening thresholds. The PDFs correspond to the data summarized in Tables 6 and 7. Generally, the PDFs change very little for the QF=0 data over ocean and land. The PDFs essentially lie atop each other. The largest changes are apparent over ocean and land for the QF=1 data. The data screening reduces the negative XCO2bc-TCCON "tail" data points. These "tail" data points are apparent in Fig. 4, 5, 10, and 11.

Graphs (not shown) of the PDFs for CSNoiseRatio screening thresholds, and thresholds for the H(3D) and H(Continuum) metrics, have a visual appearance similar to the Fig. 15 graphs. The QF-=0 PDFs lie atop each other, while the QF=1 data screening reduces the negative XCO2bc-TCCON "tail" data points.

One concludes from Tables 7 and 8 and Fig. 15 that it is possible to screen the QF=1 XCO2bc data using the Distkm or CSNoiseRatio 3D metrics to improve the standard deviations of XCO2bc-TCCON, and to reduce the XCO2bc-TCCON PDF averages to the 0.5 ppm level for the ocean data, yet this is done by a screening process which tosses out approximately 30 to 40 % of the converged retrieval QF=1 data points. For the land data the 0.5 (0.8) PDF average absolute value occurs in Distkm (CSNoiseRatio) data screening when 35 % of the data points are excluded. None of the screenings change the QF=1 standard deviations to those approaching the 0.8 ppm and 1.2 ppm standard deviations of the ocean and land QF=0 data.

11 Mitigation by additional linear-regression terms

The possibility of mitigating 3D cloud biases by adding terms to the bias correction process, was investigated by adding one or more 3D metrics to Eqns. (1)-(3). Each application of the Interactive Data Language (IDL) Regress linear regression routine solved for new Eqns. (2) and (3) linear coefficients, and new XCO2bc-TCCON standard deviations and PDF averages.

Table 9 presents representative comparisons of the two sets of calculations. Available data points, for which Distkm values were well determined for 60° S to 60° N, were used in the generation of Table 9. Two vertically adjacent numbers are tabulated for the QF=1 data. The top number is the value calculated when all possible data points are included in the regressions, while for the bottom entry the ranges of dPsco2 and CO2graddel (for oecan) and dPfrac, CO2graddel, and logDWS (for land) are equal to those ranges for the QF=0 data. The QF=0 (best quality) data points follow from the operational methodology of limiting dPsco2, DPfrac, CO2graddel (and other variables) to narrow limited ranges (see Version 9 OCO-2 Data Product User's Guide (2018) for a discussion of these ranges), The two vertically adjacent entries therefore indicate the sensitivity of the XCO2bc-TCCON XCO2 PDF standard deviations to the dPsco2, DPfrac, CO2graddel range limits.

The number of data points for the regression, the standard deviation of the XCO2bc-TCCON differences (based upon the new set of regression coefficients), and also an additional "maxlatDiff" metric are tabulated. PDF XCO2bc-TCCON averages are not presented in Table 9 since they are close to zero for all regression calculations. The "latmaxDiff" metric is calculated by first calculating XCO2bc-TCCON averages for 20º latitude bands from 60º S to 60º N, and then calculating maxlatDiff as the difference in the maximum and minimum of the five averages. If the bias correction is accurate globally, then the XCO2bc-TCCON averages should have little latitudinal variation. If this is not the case, then the latitudinal gradients associated with bias correction introduce XCO2bc latitudinal gradients (large maxldatDiff values) that will be problematic for those using OCO-2 XCO2bc to infer regional CO_2 vertical fluxes in "flux inversion" modeling studies.

Adding Distkm, H(3D), CSNoiseRatio, and H(Continuum) variables individually to the linear regressions does not significantly produce smaller XCO2bc-TCCON standard deviations or smaller maxlatDiff values, compared to the regressions that do not include these additional terms. The largest differences in Table 9 are due to imposing narrow ranges of dPsco2, dPfrac, and CO2graddel for the QF=1 data.

12 Discussion

Overall, the OCO-2 cloud pre-processor is effective in identifying clouds, but observations impacted by low altitude clouds and 3D scattering effects are sometimes not identified. The Lite files contain many observations that are close to clouds, with 40 % and 75 % of OCO-2 Lite file retrievals (see Table 2) within 4 km of clouds over the ocean and land for the QF=0 and QF=1 cases (Fig. 1). 3D radiative transfer calculations for the same cloud field (with representative surface reflectance over the ocean and land, for ocean glint and land nadir viewing geometry) indicate that 3D cloud radiance perturbations are larger over the ocean than over land (Fig. 2) at this cloud distance.

There is a marked contrast in the Lite file QF=0 and QF=1 OCO-2 data. Fig. 1 and 4 indicate that QF=1 data points are closer to clouds on average than the QF=0 data points. Fig. 4 visually indicates that there is a strong asymmetry in XCO2bc-TCCON, with more negative values than positive values for a small nearest cloud distances. Though both sets of measurements reached convergence in the operational retrieval, only the QF=0 data points are used in operational post-retrieval bias correction calculations.

From a pragmatic perspective, it is important to consider a variety of 3D cloud metrics, since the Distkm and H(3D) metrics require the processing of auxiliary MODIS cloud and radiance fields. The CSNoiseRatio and H(Continuum) metrics are calculated from *stand-alone* OCO-2 measurements. Furthermore, OCO-2 views the Earth's surface six minutes before MODIS Aqua, so some clouds observed by MODIS may not be present when OCO-2 makes observations. For a representative wind speed of 5 m/s, a cloud moves 1.8 km in six minutes, which is similar to the size of an OCO-2 footprint. The Distkm metric is a cloud field metric, while the H(3D), CSNoiseRatio, and H(Continuum) metrics are measures of radiance field inhomogeneity. Surface reflectivity variations, variations not related to 3D cloud radiative effects, contribute to all three of these radiance field metrics.

Figures 6 and 7 indicate that the Version 10 bias-corrected retrievals have a non-zero residual 3D cloud bias. The XCO2bc-TCCON averages become more negative as the nearest cloud distance decreases, and as the CSNoiseRatio increases. From Table 5,

825 XCO2bc –TCCON values at small cloud distances differ from those at large cloud distances by -0.4 and -2.2 ppm for the QF=0 and QF=1 data over the ocean. The difference in the averages at small and large cloud distances is referred to as the *cloud bias*.

While the previous discussion pertains to global statistics, 3D cloud effects are readily apparent at local scales of several degrees of longitude and latitude. This is illustrated by 830 Fig. 9, in which nearest cloud distance, H(Continuum), and Quality Flag data is presented on a footprint by footprint basis. QF=1 and larger H(Continuum) values are located right next to clouds. Fig. 10 presents XCO2bc as a function of nearest cloud distance for a larger region containing the local region presented in Fig. 9. The asymmetry in XCO2bc is readily apparent in Fig. 10, consistent with the asymmetry present in Fig. 4. The bottom panel of 835 Fig. 10 illustrates for QF=1 spectra that there is a $\pm$ 15 % variation in radiance, compared to the "Mid" radiance values, in the O_2 A-band for this scene. 3D cloud radiative perturbations are large for all three OCO-2 spectral bands.

The operational retrieval iteratively solves for a state vector (which includes surface pressure, aerosol, surface reflectance, the CO_2 vertical profile, and other variables) that 840 matches observed and forward model radiances. Since 3D cloud effect perturbations, illustrated in Fig. 10, are not incorporated into the operational retrieval, the surface pressure, aerosol, surface reflectance, and CO_2 vertical profile, will differ from the actual atmospheric values. These differences increase as the severity of the 3D cloud effect increases at small cloud distances. This is apparent in Fig. 11 in which ocean bias correction 845 (dPsco2, CO2graddel), land bias correction (DWS, and CO2graddel), and other variables (surface reflectance, and CSNoiseRatio) increase as the nearest cloud distance decreases for the QF=1 data. These variables have a much larger range in value than for the QF=0 data.

Figure 15 displays XCO2bc-TCCON PDFs calculated for a set of nearest cloud 850 thresholds from 0 to 15 km. A 5 km threshold means that only XCO2bc data with nearest cloud distances *greater* than 5km are utilized. For the QF=0 data the PDFs essentially lie atop each other. *Data screening* (see Tables 6 and 7) does not reduce the XCO2bc-TCCON averages for QF=0 data, since they are low (less than 0.5 ppm in absolute value, for ocean and land data) for data populations which include all observations. For the QF=1 data, the 855 PDFs have negative XCO2bc-TCCON tails. Tables 7 and 8 indicate that the QF=1 3D cloud biases can be reduced to the 0.5 ppm level over the ocean if approximately 60 % (70 %) of the QF=1 data points are utilized, by applying Distkm (CSNoiseRatio) metrics in a data screening process. Over land the QF=1 3D cloud biases can be reduced to the 0.5 ppm level if approximately 65 % of the QF=1 data points are utilized, by data screening 860 based upon the Distkm metric, and to the 0.8 ppm level if 63 % of the QF=1 data points are utilized based upon CSNoiseRatio data screening.

Comparing the three mitigation techniques: a) Table look-up (Section 9), b) data screening (Section 10), and c) linear-regression (Section 11), adding terms to the linear-regression equations had the least beneficial improvement in XCO2bc-TCCON statistics. 865 The Table look-up and data screening techniques both are able to reduce XCO2bc-TCCON QF=1 averages to the 0.5 ppm level. The Table look-up technique that uses two 3D metrics (Distkm and CSNoiseRatio, see Fig. 12) provides the best reduction in 3D cloud bias.

The Table Look-up technique is based upon data (see Fig. 12) that has bin to bin variations. Some of the data bins in fact have zero input data points. The bin to bin 870 variability introduces some noise to the correction process. Some of the bin to bin variation

is likely due to the fact that the retrieval code response to radiative perturbations, for physics not included in the retrieval physics, is complicated and noisy.

One advantage of the Table look-up technique, compared to the data screening technique, is that data points are not thrown out from localized scenes. This is especially useful for regions in the tropics that have relatively few OCO-2 retrievals. Table look-up (Fig. 6, 7 and 12) and 3D metrics (Distkm, H(3D), H(Contimuum), CSNoiseRatio for Lite file observations) will be placed in publically available data files. These data files can be used in application of the techniques discussed in this paper (or by other user-developed techniques) to mitigate the 3D cloud effects that are present in OCO-2 XCO2 data.

Data availability. The TCCON data can be obtained from the TCCON Data Archive hosted by CaltechDATA at https://tccondata.org. The 3D metrics (based upon Version 9 and 10 data), corresponding to Lite file observations, and associated data (such as Fig. 6, 7 and 12, which apply to version 10 OCO-2 data), can be downloaded from the CERN based Zenodo archive (https://doi.org/10.5281/zenodo.4008765).

Author Contribution. Steven Massie performed many of the calculations presented in this paper, and was the primary author of the text. Heather Cronk created the CSU MODIS files. Aronne Merrelli created the colorslice derived metrics and produced the merged data sets that combined the OCO-2 XCO2, TCCON, and 3D metrics into convenient single files. Christopher O'Dell prepared data files of TCCON and OCO-2 data that were utilized by Aronne Merrelli. Sebastian Schmidt and Hong Chen provided suggestions on the content of the paper. David Baker provided suggested modifications and clarifications in the text.

Competing interests. The authors declare that they have no conflict of interest.

Acknowledgements. STM, KSS, and HC acknowledges support by NASA Grant 80NSSC18K0889 "Towards Detection and Mitigation of 3D Cloud Effects and XCO2 Retrievals". AM acknowledges support by NASA Grants NNX15AH96G and 80NSSC18K0891. Appreciation is expressed to the TCCON teams who measure and provide ground based XCO2 validation to the carbon cycle research community. Appreciation is expressed to the OCO-2 computer staff at the Jet Propulsion Laboratory, and to Garth D'Attillo and Timothy Fredrick of the Atmospheric Chemistry Observations and Modeling (ACOM) division at the National Center for Atmospheric Research (NCAR), supported by the National Science Foundation, for maintaining the operational capabilities of computer systems during 2020, a challenging year due to the ongoing global COVID-19 pandemic.

Acronyms

ABSCO	OCO-2 and OCO-3 absorption coefficient spectroscopic database
ASTER	Advanced Spaceborne Thermal Emission and Reflection experiment
ATBD	Algorithm Theoretical Basis Document
A-train	NASA constellation of polar inclination satellites
BRDF	bidirectional diffuse reflectance

	CO2graddel	CO_2 vertical profile gradient delta
	CSNoiseRatio	Colorslice Noise Ratio
	CSU	Colorado State University
920	Distkm	nearest cloud distance (km)
	DWS	sum of Dust, Water, and Seasalt aerosol optical depths
	dPfrac	bias equation term, see equation (4), based upon the ratio of the apriori and retrieved surface pressure, and the retrieved (raw) XCO2
925	dPsco2	difference between retrieved and apriori suface pressure evaluated at the sco2 band longitude and latitude observation point
	Feats	feature bias term in the bias equation (1)
	Foot(fp)	footprint bias term in the bias equation (1)) for detector fp
	GEOS	NASA Goddard Earth Observing System model
930	GES DISC	NASA Goddard Earth Sciences Data and Information Services Center
	H(Continuum)	measured radiance field inhomogeneity metric based on the O_2 A-band continuum radiances of three rows of detectors
	H(3D)	measured radiance field inhomogeneity metric based on the MODIS 250m radiance field
935		
	IDL	Interactive Data Language computer programming language
	IPA	Independent Pixel Approximation
	Kcir	averaging circle radii index for radii of 5, 10, 15, and 20 km
	Lev1b	level 1b data file
940	Lite	OCO-2 level 2 data file that just contains successful retrievals
	logDWS	natural logarithm of DWS
	L2DiaGL	glint view level 2 diagnostic data file
	L2DiaND	nadir view level 2 disgnostic data file
	maxlatDiff	difference in the maximum and minimum of XCO2bc-TCCON averages for 20° latitude bins
945		
	MODIS	Moderate Resolution Imaging Sspectroradiometer
	OCO-2	the second Orbiting Carbon Observatory
	Papriori	apriori surface pressure
	PDF	probability distribution function
950	Pretrieved	retrieved (raw) surface pressure
	Radobs	observed O_2 A-band continuum radiance
	QF	XCO2 quality flag (0=best data, 1=lesser quality data)
	SCO2	OCO-2 strong CO_2 band
	SHDOM	Spherical Harmonic Discrete Ordinate radiative transfer Method
955	TCCON	Total Carbon Column Observation Network
	TCCONadj	equation (1) bias correction adjustment divisor
	WCO2	OCO-2 weak CO_2 band
	XCO2	column averaged atmospheric CO_2 dry air mole fraction
	XCO2bc	biased corrected XCO2
960	XCO2raw	retrieved (raw) XCO2
	XCO2bc,corr	3D cloud effect corrected XCO2bc
	XCO2raw,corr	3D cloud effect corrected XCO2raw

1D	One dimensional
3D	Three dimensional

965

References

Blumenstock, T., Hase, F., Schneider, M., Garcia, O. E., and Sepulveda, E.: TCCON data from Izana (ES), Release GGG2014.R0, TCCON Data Archive, hosted by CaltechDATA, 970 https://doi.org/10.14291/tccon.ggg2014.izana01.R0/1149295, 2014.

Connor, B., Bösch, H., McDuffie, J. Taylor, T., Fu, D., Frankenberg, C., O'Dell, C., Payne, V. H., Gunson, M., Pollock, R., Hobbs, J., Oyafuso , F., and Jiang, Y.: Quantification of uncertainties in OCO-2 measurements of XCO2: simulations and linear error analysis, 975 Atmos. Meas. Tech., 9, 5227-5238, www.atmos-meas-tech.net/9/5227/2016/doi:10.5194/ant-9-5227-2016, 2016.

Crisp, D., Pollock, H. R., Rosenberg, R., Chapsky, L., Lee, R. A. M., Oyafuso, F. A., Frankenberg, C., O'Dell, C. W., Bruegge, C. J., Doran, G. B., Eldering, A., Fisher, B. M., 980 Fu, D., Gunson, M. R., Mandrake, L., Osterman, G. B., Schwandner, F. M., Sun, K., Taylor, T. E., Wennberg, P. O., and Wunch, D.: The on-orbit performanceoftheOrbitingCarbonObservatory-2(OCO-2)instrument and its radiometrically calibrated products, Atmos. Meas. Tech.,10,59–81,https://doi.org/10.5194/amt-10-59-2017, 2017.

985

Cronk, H. OCO-2/MODIS Collocation Products User Guide, Version 3, June 2018, available at ftp://ftp.cira.colostate.edu/ftp/TTaylor/publications/, 2018.

De Mazière, M., Sha, M. K., Desmet, F., Hermans, C., Scolas, F., Kumps, N., Metzger, J.-990 M., Duflot, V., and Cammas, J.-P.: TCCON data from Réunion Island (RE), Release GGG2014.R0, TCCON Data Archive, hosted by CaltechDATA, https://doi.org/10.14291/tccon.ggg2014.reunion01.R0/1149288, 2014.

Deutscher, N. M., Notholt, J., Messerschmidt, J., Weinzierl, C., Warneke, T., Petri, C., 995 Grupe, P., and Katrynski, K.: TCCON data from Bialystok (PL), Release GGG2014.R1, TCCON Data Archive, hosted by CaltechDATA, https://doi.org/10.14291/tccon.ggg2014.bialystok01.R1/1183984, 2015.

Eldering, A., O'Dell, C. W., Wennberg, P. O., Crisp, D., Gunson, M. R., Viatte, C., Avis, 1000 C., Braverman, A., Castano, R., Chang, A., Chapsky, L., Cheng, C., Connor, B., Dang, L., Doran, G., Fisher, B., Frankenberg, C., Fu, D., Granat, R., Hobbs, J., Lee, R.A.M., Mandrake, L., McDuffie, J., Miller, C. E., Myers, V., Natraj, V., O'Brien, D., Osterman, G. B., Oyafuso, F., Payne, V. H., Pollock, H.R., Polonsky, I., Roehl, C.M., Rosenberg, R., Schwandner, F., Smyth, M., Tang, V., Taylor, T. E., To, C., Wunch, D., and Yoshimizu, 1005 J.: The Orbiting Carbon Observatory-2: first 18 months of science data products, Atmos. Meas. Tech., 10, 549– 563, https://doi.org/10.5194/amt-10-549-2017, 2017.

Evans, K.F.: The spherical harmonics discrete ordinate method for three-dimensional atmospheric radiative transfer, Atmos. Sci., 55, 429–446, 1998.

1010

Genkova, I., Seiz, G., Zuidema, P., Zhao, G., and Di Girolamo, L.: Cloud top height comparisons from ASTER, MISR, and MODIS for trade wind cumuli, Rem. Sen. Env., 107, 211-222, 2007.

1015 Goo, T.-Y., Oh, Y.-S., and Velazco, V. A.: TCCON data from Anmeyondo (KR), Release GGG2014.R0, TCCON Data Archive, hosted by CaltechDATA, https://doi.org/10.14291/tccon.ggg2014.anmeyondo01.R0, 2014.

Griffith, D. W. T., Velazco, V. A., Deutscher, N. M., PatonWalsh, C., Jones, N. B., Wilson, 1020 S. R., Macatangay, R. C., Kettlewell, G. C., Buchholz, R. R., and Riggenbach, M.: TCCON data from Wollongong (AU), Release GGG2014.R0, TCCON Data Archive, hosted by CaltechDATA, https://doi.org/10.14291/tccon.ggg2014.wollongong01.R0, 2014.

Hase, F., Blumenstock, T., Dohe, S., Gross, J., and Kiel, M.: TCCON data from Karlsruhe 1025 (DE), Release GGG2014.R1, TCCON Data Archive, hosted by Caltech DATA, https://doi.org/10.14291/tccon.ggg2014.karlsruhe01.R1, 2015.

Iraci, L. T., Podolske, J., Hillyard, P. W., Roehl, C., Wennberg, P. O., Blavier, J.-F., Allen, N., Wunch, D., Osterman, G., and Albertson, R.: TCCON data from Edwards (US), 1030 Release GGG2014.R1, TCCON Data Archive, hosted by CaltechDATA, https://doi.org/10.14291/tccon.ggg2014.edwards01.R1/1255068, 2016.

Kawakami, S., Ohyama, H., Arai, K., Okumura, H., Taura, C., Fukamachi, T., and Sakashita, M.: TCCON data from Saga (JP), Release GGG2014.R0, TCCON Data 1035 Archive, hosted by CaltechDATA, https://doi.org/10.14291/tccon.ggg2014.saga01.R0/1149283, 2014.

Kivi, R. and Heikkinen, P.: Fourier transform spectrometer measurements of column CO_2 at Sodankylä, Finland, Geosci. Instrum. Method. Data Syst., 5, 271–279, 1040 https://doi.org/10.5194/gi-5-271-2016, 2016.

Liang, L., Di Girolamo, L., and Platnick., S.: View-angle consistency in reflectance, optical thickness and spherical albedo of marine water-clouds over the northwestern Pacific through MISR-MODIS fusion, Geo. Res. Lett., 36, L09811, doi:10.1029/2008GL037124, 1045 2009.

Lu, M.-L., McClatchey, R. A., and Seinfeld, J. H.: Cloud halos: Numerical simulation of dynamical structure and radiative impact, J. Appl. Meteorol., 41, 832 – 848, 2002.

1050 Lu, M.-L., Wang, J., Freedman, A., Jonsson, H. H., Flagan, R. C., McClatchey, R. A., and Seinfeld, J. H.: Analysis of humidity halos around trade wind cumulus clouds, J. Atmos. Sci., 60, 1041 – 1059, 2003.

Massie, S. T., Schmidt, K. S., Eldering, A., and Crisp, D.: Observational evidence of 3-D cloud effects in OCO-2 CO2 retrievals, J. Geophys. Res. Atmos., 122, doi:10.1002/2016JD026111, 2017.

Merrelli, A., Bennartz, R., O'Dell, C. W., and Taylor, T. E.: Estimating bias in the OCO-2 retrieval algorithm caused by 3-D radiation scattering from unresolved boundary layer clouds, Atmos. Meas. Tech., 8, 1641–1656, https://doi.org/10.5194/amt-8-1641-2015, 2015.

Morino, I., Matsuzaki, T., and Horikawa, M.: TCCON data from Tsukuba (JP), 125HR, Release GGG2014.R1, TCCON Data Archive, hosted by CaltechDATA, https://doi.org/10.14291/tccon.ggg2014.tsukuba02.R1/1241486, 2016a.

Morino, I., Yokozeki, N., Matsuzaki, T., and Horikawa, M.: TCCON data from Rikubetsu (JP), Release GGG2014.R1, TCCON Data Archive, hosted by CaltechDATA, https://doi.org/10.14291/tccon.ggg2014.rikubetsu01.R1, 2016b.

Notholt, J., Petri, C., Warneke, T., Deutscher, N. M., Buschmann, M., Weinzierl, C., Macatangay, R. C., and Grupe, P.: TCCON data from Bremen (DE), Release GGG2014.R0, TCCON Data Archive, hosted by CaltechDATA, https://doi.org/10.14291/tccon.ggg2014.bremen01.R0/1149275, 2014.

Orbiting Carbon Observatoruy-2 & 3 (OCO-2 & OCO-3) Level 2 Full Physics Retrieval Algorithm Theoretical Basis, Version 2.0 Rev 3 January 2, 2019.

O'Dell, C. W., Eldering, A., Wennberg, P. O., Crisp, D., Gunson, M. R., Fisher, B., Frankenberg, C., Kiel, M., Lindqvist, H., Mandrake, L., Merrelli, A., Natraj, V., Nelson, R. R., Osterman, G. B., Payne, V. H., Taylor, T. E., Wunch, D., Drouin, B. J., Oyafuso, F., Chang, A., McDuffie, J., Smyth, M., Baker, D. F., Basu, S., Chevallier, F., Crowell, S. M.R., Feng, L., Palmer, P. I., Dubey, M., Garcia, O. E., Griffith, D. W.T., Hase, F., Iraci, L. T., Kivi, R., Morino, I., Notholt, J., Ohyama, H., Petri, C., Roehl, C. M., Sha, M. K., Strong, K., Sussmann, R., Te, Y., Uchino, O. & Velazco, V. A.: Improved retrievals of carbon dioxide from Orbiting Carbon Observatory-2 with the version 8 ACOS algorithm. Atmos. Meas. Tech., 11 (12), 6539-6576, 2018.

Okata, M.., Nakajima, T., Suzuki, K., Jnoue, T., Nakajima, T. Y., and Okamato, H.: A study on radiative transfer effects in 3-D cloudy atmosphere using satellite data, J. Geophys. Res. Atmos., 122, 443–468, doi:10.1002/2016JD025441, 2017.

Orbiting Carbon Observatory–2 (OCO-2) Data Product User's Guide, Operational L1 and L2 Data Versions 8 and Lite File Version 9, Version 1, Revision J., October 10, 2018, https://docserver.gesdisc.eosdis.nasa.gov/public/project/OCO/OCO-2_DUG.V9.pdf , 2018.

Orbiting Carbon Observatory–2 & 3 (OCO-2 & OCO-3) Data Product User's Guide, Operational Level 2 Data Versions 10 and VEarly, Version 1, Revision A., June 8,

1100 2020,https://docserver.gesdisc.eosdis.nasa.gov/public/project/OCO/OCO2_OCO3_B 10_DUG.pdf, 2020.

Payne, V.: ABSCO User Guide, JPL Document, March 18, 2016.

1105 Pincus, R., and Evans, K. F.: Computational cost and accuracy in calculating three-dimensional radiative transfer: Results for new implementations of Monte Carlo and SHDOM, J. Atmos. Sci., 66, 3131–3146, 2009.

Rayner, P. J., and O'Brien, D. M.: The utility of remotely sensed CO_2 concentration data
1110 insurface source inversions, Geophys. Res. Lett., 28, 175–178, doi:10.1029/2000GL011912, 2001.

Rodgers, C. D.: Inverse Methods for Atmospheric Sounding: Theory and Practice, World Scientific, Singapore, 2000.
1115
Sherlock, V., Connor, B., Robinson, J., Shiona, H., Smale, D., and Pollard, D.: TCCON data from Lauder (NZ), 125HR, Release GGG2014.R0, TCCON Data Archive, hosted by CaltechDATA, https://doi.org/10.14291/tccon.ggg2014.lauder02.R0/1149298, 2014.

1120 Sussmann, R. and Rettinger, M.: TCCON data from Garmisch (DE), Release GGG2014.R0, TCCON Data Archive, hosted by CaltechDATA, https://doi.org/10.14291/tccon.ggg2014.garmisch01.R0/1149299, 2014.

Te, Y., Jeseck, P., and Janssen, C.: TCCON data from Paris (FR), Release GGG2014.R0,
1125 TCCON Data Archive, hosted by CaltechDATA, https://doi.org/10.14291/tccon.ggg2014.paris01.R0/1149279, 2014.

Twohy, C. H., Coakley Jr., J. A., and W. R. Tahnk, W. R.: Effect of changes in relative humidity on aerosol scattering near clouds, J. Geophys. Res., 114, D05205,
1130 doi:10.1029/2008JD010991, 2009.

Várnai, T., and Marshak, A.: MODIS observations of enhanced clear sky reflectance near clouds, Geophys. Res. Lett., 36, L06807, doi:10.1029/2008GL037089, 2009.

1135 Velazco, V., Morino, I., Uchino, O., Hori, A., Kiel, M., Bukosa, B., Deutscher, N., Sakai, T., Nagai, T., Bagtasa, G., Izumi, T., Yoshida, Y., and Griffith, D.: TCCON Philippines: First Measurement Results, Satellite Data and Model Comparisons in Southeast Asia, Remote Sens., 9, 1228, https://doi.org/10.3390/rs9121228, 2017.

1140 Warneke, T., Messerschmidt, J., Notholt, J., Weinzierl, C., Deutscher, N. M., Petri, C., Grupe, P., Vuillemin, C., Truong, F., Schmidt, M., Ramonet, M., and Parmentier, E.: TCCON data from Orléans (FR), Release GGG2014.R0, TCCON Data Archive, hosted by CaltechDATA, https://doi.org/10.14291/tccon.ggg2014.orleans01.R0/1149276, 2014.

1145 Wennberg, P. O., Roehl, C., Wunch, D., Toon, G. C., Blavier, J.-F., Washenfelder, R., Keppel-Aleks, G., Allen, N., and Ayers, J.: TCCON data from Park Falls (US), Release GGG2014.R0, TCCON Data Archive, hosted by CaltechDATA, https://doi.org/10.14291/tccon.ggg2014.parkfalls01.R0/1149161, 2014.

1150 Wennberg, P. O., Wunch, D., Roehl, C., Blavier, J.-F., Toon, G. C., and Allen, N.: TCCON data from Caltech (US), Release GGG2014.R1, TCCON Data Archive, hosted by CaltechDATA, https://doi.org/10.14291/tccon.ggg2014.pasadena01.R1, 2015.

       Wennberg, P. O., Wunch, D., Roehl, C., Blavier, J.-F., Toon, G. C., and Allen, N.: TCCON
1155 data from Lamont (US), Release GGG2014.R1, TCCON Data Archive, hosted by CaltechDATA, https://doi.org/10.14291/tccon.ggg2014.lamont01.R1/1255070, 2016.

       Wunch, D., Toon, G. C., Wennberg, P. O., Wofsy, S. C., Stephens, B. B., Fischer, M. L., Uchino, O., Abshire, J. B., Bernath, P., Biraud, S.C., Blavier, J.-F.L., Boone, C., Bowman,
1160 K.P., Browell, E. V., Campos, T., Connor, B. J., Daube, B. C., Deutscher, N. M., Diao, M., Elkins, J. W., Gerbig, C., Gottlieb, E., Griffith, D. W. T., Hurst, D. F., Jiménez, R., Keppel-Aleks, G., Kort, E. A., Macatangay, R., Machida, T., Matsueda, H., Moore, F., Morino, I., Park, S., Robinson, J., Roehl, C. M., Sawa, Y., SherLock, V., Sweeney, C., Tanaka, T., and Zondlo, M. A.: Calibration of the Total Carbon Column Observing Network using aircraft
1165 profile data, Atmos. Meas. Tech., 3, 1351–1362, https://doi.org/10.5194/amt-3-1351-2010, 2010.

       Wunch, D., Toon, G. C., Sherlock, V., Deutscher, N. M., Liu, C., Feist, D. G., & Wennberg, P. O. (2015). Documentation for the 2014 TCCON Data Release (Version
1170 GGG2014.R0). *CaltechDATA*. https://doi.org/10.14291/tccon.ggg2014.documentation.r0/1221662).

       Wunch, D., Mendonca, J., Colebatch, O., Allen, N. T., Blavier, J.-F., Springett, S., Neufeld, G., Strong, K., Kessler, R., and Worthy, D.: TCCON data from East Trout Lake, SK (CA),
1175 Release GGG2014.R0, TCCON Data Archive, hosted by CaltechDATA, https://doi.org/10.14291/tccon.ggg2014.easttroutlake01.R0, 2016.

       Wunch, D., Wennberg, P. O., Osterman, G., Fisher, B., Naylor, B., Roehl, C. M., O'Dell, C., Mandrake, L., Viatte, C., Kiel, M., Griffith, D. W. T., Deutscher, N. M., Velazco, V.
1180 A., Notholt, J., Warneke, T., Petri, C., De Maziere, M., Sha, M. K., Sussmann, R., Rettinger, M., Pollard, D., Robinson, J., Morino, I., Uchino, O., Hase,F., Blumenstock,T., Feist, D.G., Arnold, S.G., Strong, K., Mendonca, J., Kivi, R., Heikkinen, P., Iraci, L., Podolske, J., Hillyard, P. W., Kawakami, S., Dubey, M. K., Parker, H. A., Sepulveda, E., García, O. E., Te, Y., Jeseck, P., Gunson, M. R., Crisp,D., and Eldering,A.: Comparisons
1185 of the Orbiting Carbon Observatory-2 (OCO-2) XCO2 measurements with TCCON, Atmos. Meas. Tech., 10, 2209–2238, https://doi.org/10.5194/amt10-2209-2017, 2017.

Table 1. List of TCCON sites and their locations.

	Site	Latitude	Longitude	Reference
1190	Anmyeondo, Korea	36.53	126.33	Goo et al. (2014)
	Armstrong, USA	34.59	-117.88	Iraci et al. (2016)
	Bialystok, Poland	53.23	23.02	Deutscher et al. (2015)
1195	Bremen, Germany	53.10	8.85	Notholt et al. (2014)
	Borgos, Philippines	18.53	120.65	Velazco et al. (2017)
	Caltech, USA	34.13	-118.12	Wennberg et al. (2015)
	East Trout Lake, Canada	54.35	-104.98	Wunch et al. (2016)
	Garmisch, Germany	47.47	11.06	Sussmann, Rettinger (2014)
1200	Izana, Tenerife	28.3	-16.5	Blumenstock et al. (2014)
	Karlsruhe, Germany	49.10	8.43	Hase et al. (2015)
	Lamont, OK, USA	36.60	-97.48	Wennberg et al. (2016)
	Lauder, New Zealand	-45.03	169.68	Sherlock et al. (2014)
	Orleans, France	47.97	2.11	Warneke et al. (2014)
1205	Paris, France	48.84	2.35	Te et al. (2014)
	Park Falls, WI, USA	45.94	-90.27	Wennberg et al. (2014)
	Réunion Island	-20.90	55.48	De Mazière et al. (2014)
	Rikubetsu, Japan	43.45	143.76	Morino et al. (2016b)
	Saga, Japan	33.24	130.28	Kawakami et al. (2014)
1210	Sodankyla, Finland	67.36	26.63	Kivi and Heikkinen (2016)
	Tsukuba, Japan	36.05	140.12	Morino et al. (2016a)
	Wollongong, Australia	-34.40	150.87	Griffith et al. (2014)

Table 2. The fractions of OCO-2 Lite file observations (in percent) that have a cloud
within 4 km of an observation footprint for each season.[a]

Season	Ocean, QF=0	Land, QF=0	Ocean, QF=1	Land, QF=1
Winter[b]	30-54	30-53	61-90	61-96
Average	37	42	79	77
Spring	32-55	31-53	73-88	60-83
Average	42	42	80	73
Summer	30-57	29-56	59-89	58-82
Average	41	39	79	70
Fall	21-58	24-55	55-88	59-83
Average	41	38	78	70

[a]The two tabulated numbers are the minimum and maximum values of the fractions (in
%) for five 20º latitudinal bins (see Fig. 1). The Average value is the average of the
fractions of the latitudinal bins.
[b]Winter corresponds to December – February, Spring to March – May, Summer to June –
August, and Fall to September – November.

1215
1220
1225
1230
1235

1240

Table 3. Input to SHDOM calculations.[a]

Variable	Base State	Perturbation

1245

| Surface Pressure (hPa) | 1016 | 1026 |
| Surface Reflectance (nadir) | 0.32, 0.21, 0.11 | 0.35, 0.23, 0.12 |

1250

Wind velocity (glint)	10, 10, 10 m sec^{-1}	15, 15, 15 m sec^{-1}
Aerosol Optical Depth	0,11, 0.06, 0.048	0.165, 0.09, 0.072
CO_2 (ppm)	400	410

1255

----

[a]The triplet of numbers refer to the O2, WCO2, and SCO2 bands, respectively. Perturbations are applied individually one at a time, keeping all other variables to their base state values.

1260

Table 4. Minimum standard deviations (ppm) and ranges of the ratios of the Version 10 XCO2-TCCON standard deviations.[a]

Metric	Ocean, QF=0	Land, QF=0	Ocean, QF=1	Land, QF=1
Minimum standard deviations				
Cloud Distance	1.04 (raw)	1.75	1.64	2.79
	0.76 (bc)	1.20	1.45	2.18
H(3D)	0.98	1.62	1.95	2.57
	0.69	1.03	1.91	1.73
CSNoiseRatio	1.04	1.68	2.02	2.69
	0.79	1.11	1.78	2.28
H(Continuum)	0.98	1.45	1.74	1.91
	0.72	0.96	1.18	1.97
Ranges of the standard deviation ratios[b]				
Metric	Ocean, QF=0	Land, QF=0	Ocean, QF=1	Land, QF=1
Cloud Distance	1.16 (raw)	1.14	1.41	1.26
	1.26 (bc)	1.19	1.62	1.70
H(3D)	1.20	1.79	1.20	1.45
	1.43	1.70	1.23	2.08
CSNoiseRatio	1.22	1.14	1.25	1.37
	1.74	1.11	1.52	1.51
H(Continuum)	1.36	1.52	1.55	2.00
	1.43	1.53	2.36	1.70

[a]The pairs of numbers refer to raw and bias corrected (bc) XCO2.
[b]The range of the standard deviation ratios is the maximum standard deviation divided by the minimum standard deviation of the set of standard deviations for a given metric, surface type, and QF flag.

Table 5. 3D cloud biases for bias corrected V9 and V10 XCO2.[a]

Metric	Ocean, QF=0	Ocean, QF=1	Land, QF=0	Land, QF=1
Cloud Distance	-0.5 (V9)	-2.5	0.05	-3.3
	-0.4 (V10)	-2.2	±0.1	-2.5
H(3D)	±0.5	±1.6	±1	±2
	±0.3	±2.0	0.4	±2.2
CSNoiseRatio	-1.5	-1.9	0.3	-1
	-1.3	-1.4	0.15	-0.9
H(Continuum)	-0.8	-2.0	0.5	±5
	-0.4	-1.5	0.5	±3.7

[a] There are two paired numbers. The top number is for Version 9 data, while the bottom number is for Version 10 data. A negative 3D cloud bias indicates that XCO2bc is less than TCCON XCO2. A ± value indicates that the graph of e.g. H(3D) versus XCO2bc – TCCON is not monotonic (i.e. there is a maximum or minimum of the graph in the middle of the graph). The cloud biases are read off from inspection of Fig. 6 and 7 (i.e. the range in y axis values) and corresponding graphs of x=H(3D), CSNoiseRatio or H(Continuum) versus y= XCO2bc – TCCON in other graphs (not shown).

1310

1315

1320

1325

1330

1335 Table 6. Statistics of the single variable Table look-up cloud bias mitigation calculations.[a]

Metric		Ocean, QF=0	Ocean, QF=1	Land, QF=0	Land, QF=1
1340 Standard	bc stnd	0.83	2.33	1.21	3.88
	bc ave	0.30	-0.98	0.11	-1.06
Distkm	raw stnd	1.09	2.32	1.80	3.64
	bc stnd	0.82	2.19	1.21	3.78
1345	raw ave	0.02	0.00	0.00	0.07
	bc ave	0.00	0.01	-0.02	0.08
H(3D)	raw stnd	1.06	2.36	1.74	3.48
1350	bc stnd	0.80	2.21	1.15	3.56
	raw ave	0.09	0.12	-0.21	-0.18
	bc ave	0.02	-0.04	-0.11	-0.06
1355 CSNoiseRatio	raw stnd	1.06	2.39	1.74	3.54
	bc stnd	0.80	2.23	1.15	3.62
	raw ave	0.11	0.17	-0.13	0.10
	bc ave	0.06	0.08	-0.11	0.20
1360					
H(Continuum)	raw stnd	1.07	2.39	1.74	3.53
	bc stnd	0.81	2.26	1.15	3.62
	raw ave	0.03	0.13	-0.11	0.00
	bc ave	0.00	0.03	-0.09	0.22

1365

[a]The first two "Standard" rows of the Table refer to the standard deviations (stnd, in ppm) and averages of XCO2bc –TCCON, with XCO2bc from the Lite files. The four rows for each metric report the standard deviations and averages of XCO2raw,corr – TCCON and
1370 XCO2bc,corr – TCCON.

Table 7. Standard Deviations (in ppm) of Version 10 XCO2bc-TCCON XCO2 over the ocean for various Distkm, H(3D), H(Continuum), and CSNoiseRatio thresholds [a]

Quality flag=0

Range	Standard Deviations	PDF Average	Fraction of Data Points
0 1.0 40 20	0.84 0.81 0.81 0.81	0.31 0.32 0.32 0.32	1.00 1.00 1.00 1.00
1 0.8 30 10	0.82 0.81 0.81 0.81	0.34 0.32 0.32 0.32	0.91 0.98 0.99 1.00
2 0.6 20 8	0.80 0.80 0.81 0.81	0.36 0.33 0.33 0.32	0.83 0.95 0.98 1.00
3 0.4 15 5	0.79 0.79 0.80 0.81	0.38 0.34 0.33 0.32	0.75 0.90 0.96 1.00
5 0.3 10 3	0.78 0.78 0.80 0.81	0.40 0.36 0.33 0.33	0.62 0.85 0.93 0.99
10 0.2 5 2	0.77 0.77 0.77 0.79	0.41 0.37 0.35 0.35	0.39 0.78 0.78 0.94
15 0.1 2 1	0.77 0.77 0.72 0.77	0.41 0.40 0.40 0.41	0.24 0.66 0.31 0.51

Quality Flag =1

Range	Standard Deviations	PDF Average	Fraction of Data Points
0 1.0 40 20	2.34 2.33 2.22 2.33	-0.99 -0.84 -0.72 -0.86	1.00 1.00 1.00 1.00
1 0.8 30 10	2.12 2.31 2.17 2.24	-0.51 -0.75 -0.67 -0.79	0.60 0.91 0.95 0.96
2 0.6 20 8	2.03 2.25 2.05 2.19	-0.16 -0.54 -0.58 -0.74	0.41 0.75 0.85 0.92
3 0.4 15 5	1.96 2.09 1.96 2.07	0.09 -0.21 -0.52 -0.58	0.30 0.53 0.76 0.79
5 0.3 10 3	1.89 1.95 1.81 1.94	0.36 -0.01 -0.43 -0.38	0.19 0.41 0.60 0.58
10 0.2 5 2	1.86 1.82 1.56 1.83	0.54 0.22 -0.22 -0.21	0.11 0.31 0.30 0.40
15 0.1 2 1	1.80 1.61 1.33 1.51	0.53 0.42 0.22 0.18	0.06 0.21 0.05 0.12

----

[a] Columns 1-4 refer to Distkm, H(3D), H(Continuum), and CSNoiseRatio data screening thresholds. In the first column, "2" indicates that Distkm data from 2 to 50 km are utilized, yielding a standard deviation for QF=0 data of 0.80 (column 5), with an average PDF XCO2(bc) – T CCON XCO2 of 0.36 ppm (column 9), with a fraction of 0.83 of the total number of data points being utilized (column 13).

Table 8. Standard Deviations (in ppm) of Version 10 XCO2bc-TCCON XCO2 over land for various Distkm, H(3D), H(Continuum), and CSNoiseRatio thresholds. [a]

1410

Quality flag=0

	Range			Standard Deviations				PDF Average				Fraction of Data Points			
0	1.0	40	20	1.22	1.14	1.14	1.15	0.12	0.01	0.00	0.00	1.00	1.00	1.00	1.00
1	0.8	30	10	1.22	1.14	1.14	1.15	0.12	0.01	0.00	0.00	0.95	1.00	0.99	0.99
2	0.6	20	8	1.21	1.13	1.12	1.14	0.12	0.00	-0.00	0.00	0.91	0.99	0.94	0.97
3	0.4	15	5	1.19	1.12	1.11	1.14	0.11	-0.00	-0.01	-0.01	0.87	0.96	0.87	0.90
5	0.3	10	3	1.17	1.10	1.09	1.13	0.11	-0.01	-0.03	-0.02	0.78	0.90	0.67	0.72
10	0.2	5	2	1.14	1.05	1.05	1.12	0.09	-0.04	-0.12	-0.04	0.57	0.68	0.20	0.50
15	0.1	2	1	1.11	0.97	1.00	1.12	0.08	-0.16	-0.52	-0.12	0.39	0.16	0.01	0.08

1415

1420

Quality Flag =1

1425

	Range			Standard Deviations				PDF Average				Fraction of Data Points			
0	1.0	40	20	3.91	3.64	3.53	3.60	-1.07	-0.95	-0.94	-0.96	1.00	1.00	1.00	1.00
1	0.8	30	10	3.20	3.54	3.45	3.47	-0.69	-0.93	-0.94	-0.95	0.80	0.95	0.94	0.94
2	0.6	20	8	2.88	3.31	3.26	3.40	-0.53	-0.80	-0.89	-0.93	0.68	0.86	0.80	0.90
3	0.4	15	5	2.68	2.94	3.12	3.22	-0.42	-0.56	-0.85	-0.87	0.58	0.72	0.66	0.76
5	0.3	10	3	2.49	2.77	2.96	3.04	-0.32	-0.49	-0.84	-0.79	0.45	0.59	0.43	0.54
10	0.2	5	2	2.27	2.75	3.27	2.92	-0.28	-0.55	-1.32	-0.75	0.27	0.35	0.11	0.35
15	0.1	2	1	2.13	3.47	4.88	2.93	-0.26	-1.25	-2.74	-0.86	0.16	0.07	0.00	0.06

1430

1435

[a] Columns 1-4 refer to Distkm, H(3D), H(Continuum), and CSNoiseRatio data screening thresholds.

Table 9. Multi-variable linear regression standard deviations and maxlatDiff values.[a]

	Ocean, QF=0			Ocean, QF=1		
Variable	Number	Stnd	maxlatDiff	Number	Stnd	maxlatDiff
Standard	119144	0.86	0.46	53247	2.16	0.43
				29434	1.41	0.55
Distkm	119144	0.85	0.41	53247	2.09	0.32
				29434	1.39	0.51
H(3D)	119144	0.85	0.45	53247	2.13	0.41
				29434	1.41	0.50
CSNoiseRatio	119144	0.84	0.39	53247	2.13	0.40
				29434	1.39	0.47
H(C)	114137	0.85	0.46	53247	2.11	0.44
				29434	1.40	0.53

	Land, QF=0			Land, QF=1		
Variable	Number	Stnd	maxlatDiff	Number	Stnd	maxlatDiff
Standard	155602	1.24	0.09	113147	3.27	0.42
				91620	2.75	0.34
Distkm	155602	1.24	0.08	113147	3.24	0.55
				91620	2.73	0.43
H(3D)	154599	1.24	0.28	113044	3.23	0.39
				91518	2.75	0.42
CSNoiseRatio	155602	1.24	0.09	113147	3.25	0.54
				91620	2.74	0.49
H(C)	154582	1.23	0.10	112449	3.26	0.45
				91064	2.74	0.30

[a]"Standard" refers to multiple linear regressions in which only the Version 10 standard variables (dPsco2, co2graddel for ocean; and dPfrac, CO2graddel, aodfine and log(DWS) for land) are utilized. The lower number in the QF=1 pairs refers to calculations with a restricted range of data (similar to that for the QF=0 data) for the standard variables. Variable "Distkm" indicates taht the standard variables, plus the Distkm variable, are used

1485   in the multiple-regression calculations. "Number" refers to the number of observations used in the calculations. H(C) refers to the H(Continuum) metric.
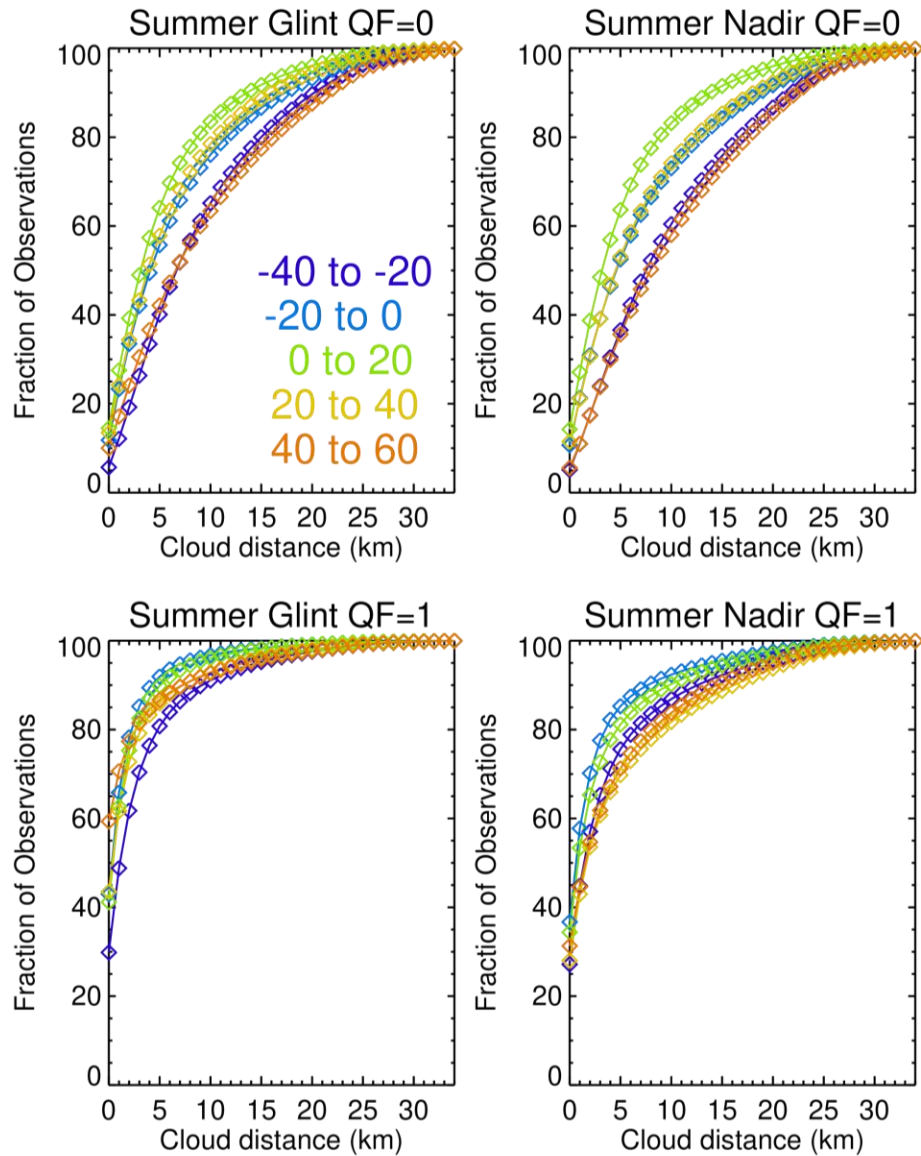
Figure 1. Fraction of observations that have a cloud within a circle of a specified radius (given by the x axis values) in summer for Ocean Glint and Land Nadir Lite file data points for QF=0 (best quality) and QF=1 (lesser quality) data. Each curve is for a labeled 20° latitudinal band. QF=1 fractions are generally larger than the QF=0 fractions.
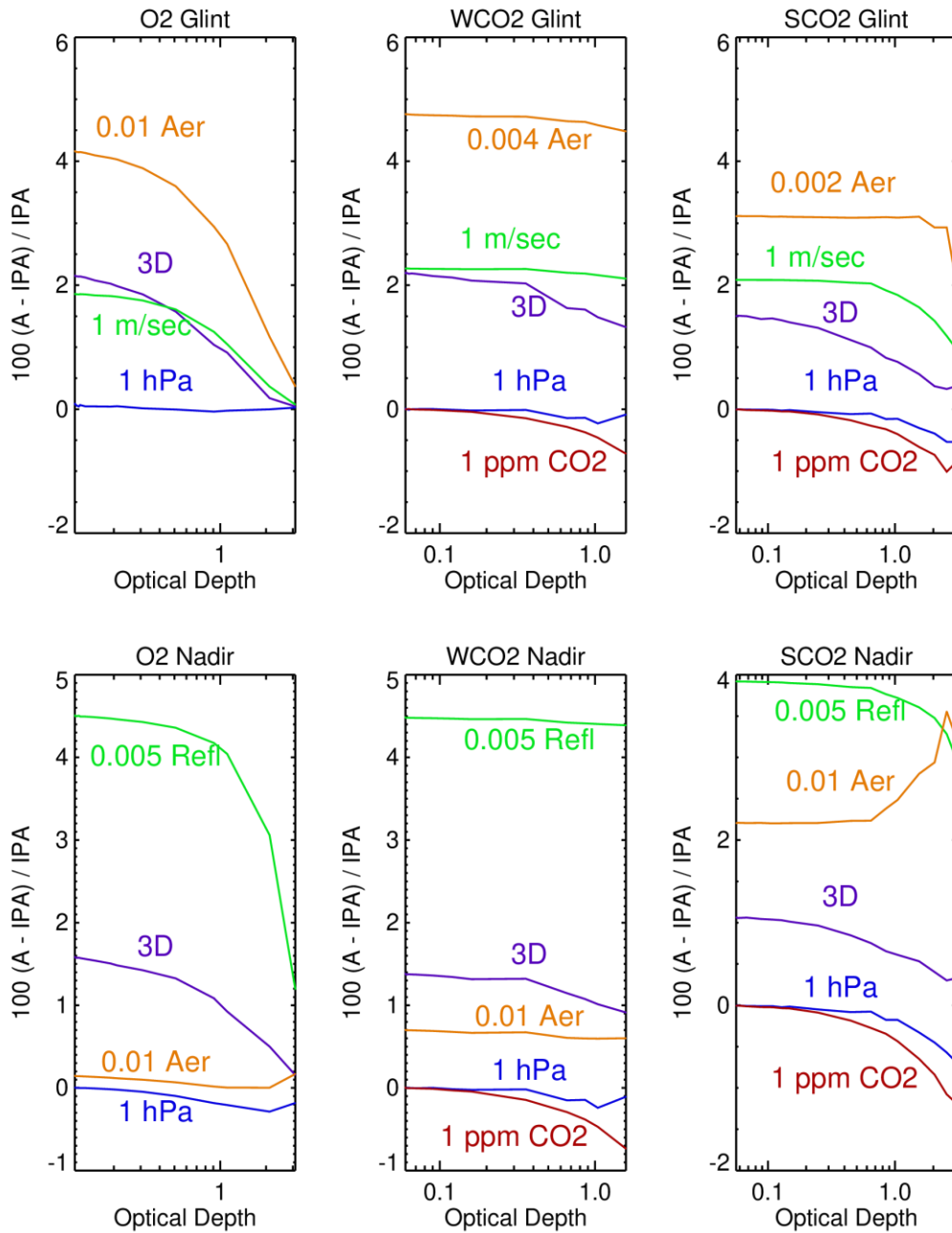
Figure 2. SHDOM 1D (IPA) and 3D radiative perturbations for ocean glint and land nadir viewing geometry using the same Fig. 9 cloud field. "A" in the y-axis title refers to 3D or 1D radiative perturbations. The 3D radiance perturbations for glint viewing geometry are larger than the nadir viewing geometry perturbations.
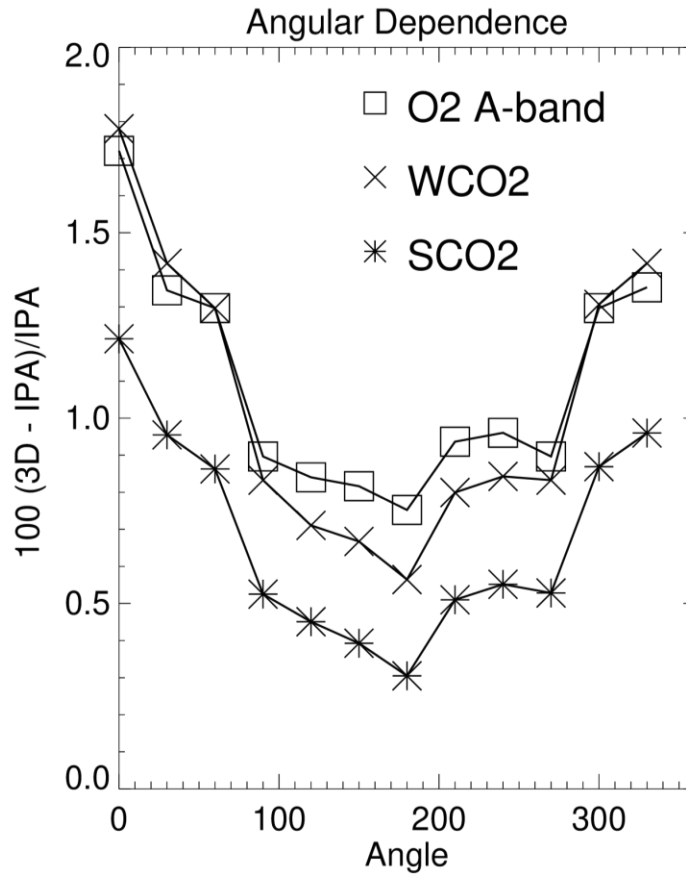
Figure 3. The angular dependence of the SHDOM 100 (3D-IPA)/IPA radiative perturbations for glint view geometry for observation footprints along a circle 4 km surrounding an isolated cloud. The observation footprints are to the west, north, east, and south of the cloud at angles of 0º, 90º, 180º and 270º. The sun is along the –x axis and the sensor is along the +x axis.

1500
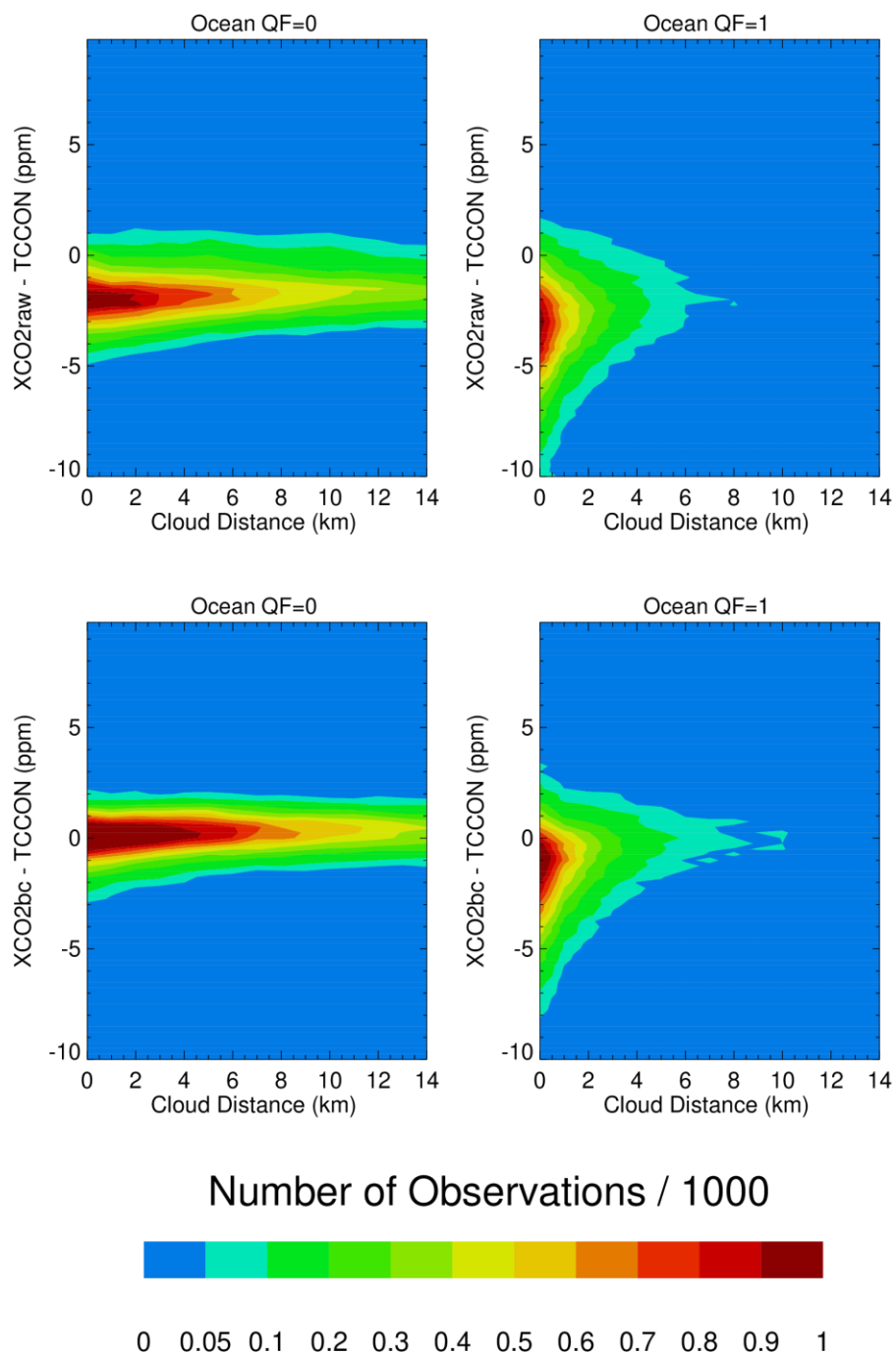
1505 **Figure 4**. Contour maps of XCO2 – TCCON over the ocean as a function of the nearest cloud distance for QF=0 and QF=1 XCO2raw and XCO2bc Version 10 data. There is a very noticeable asymmetry (a tail of negative XCO2bc-TCCON) along vertical lines of nearest cloud distance in the QF=1 data, especially for small nearest cloud distance.
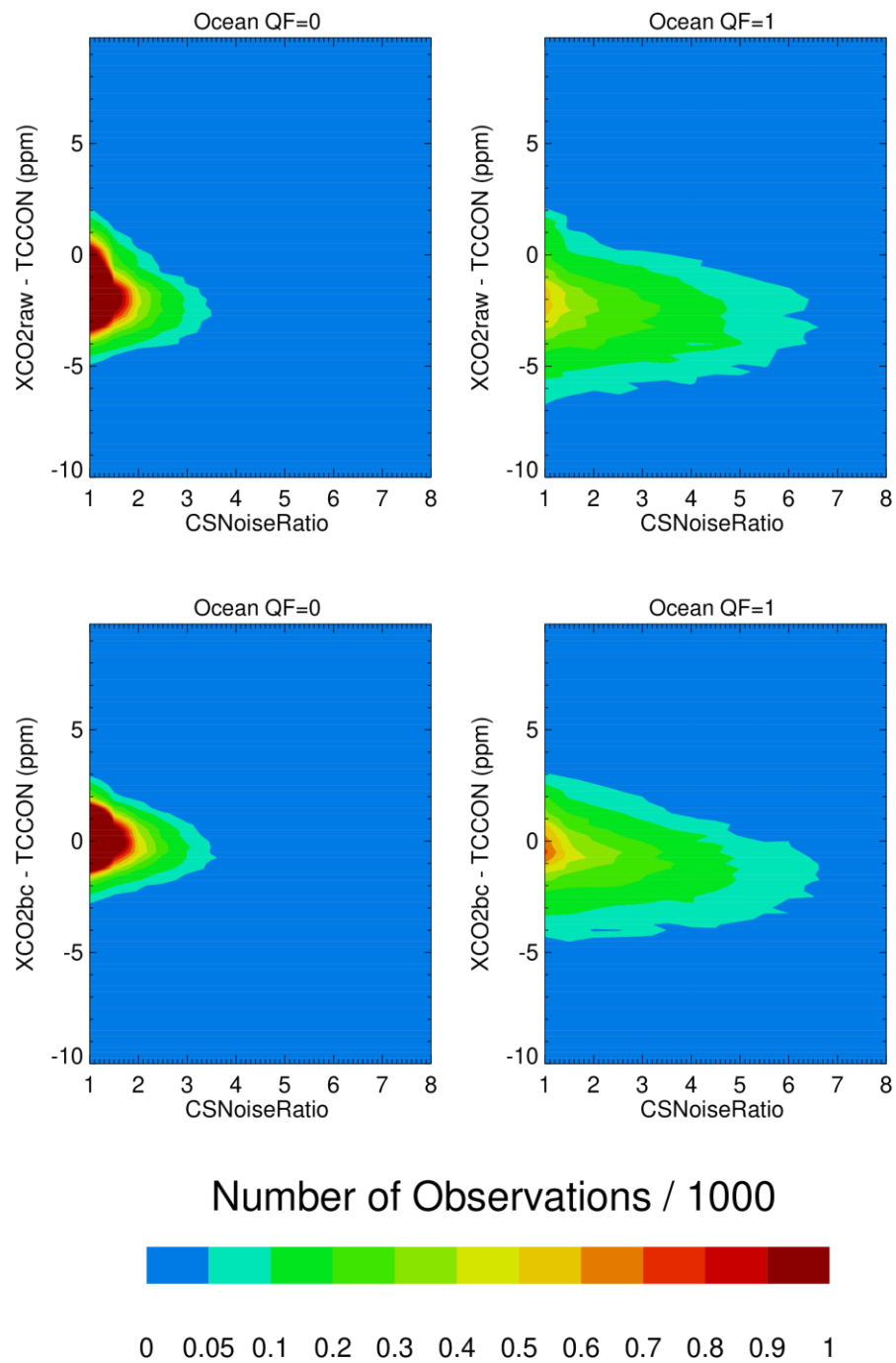
1510   **Figure 5**. Contour maps of XCO2 – TCCON over the ocean as a function of the CSNoiseRatio metric for QF=0 and QF=1 XCO2raw and XCO2bc Version 10 data. The QF=1 XCO2bc data over the ocean has a noticeable asymmetry along CSNoiseRatio vertical lines.
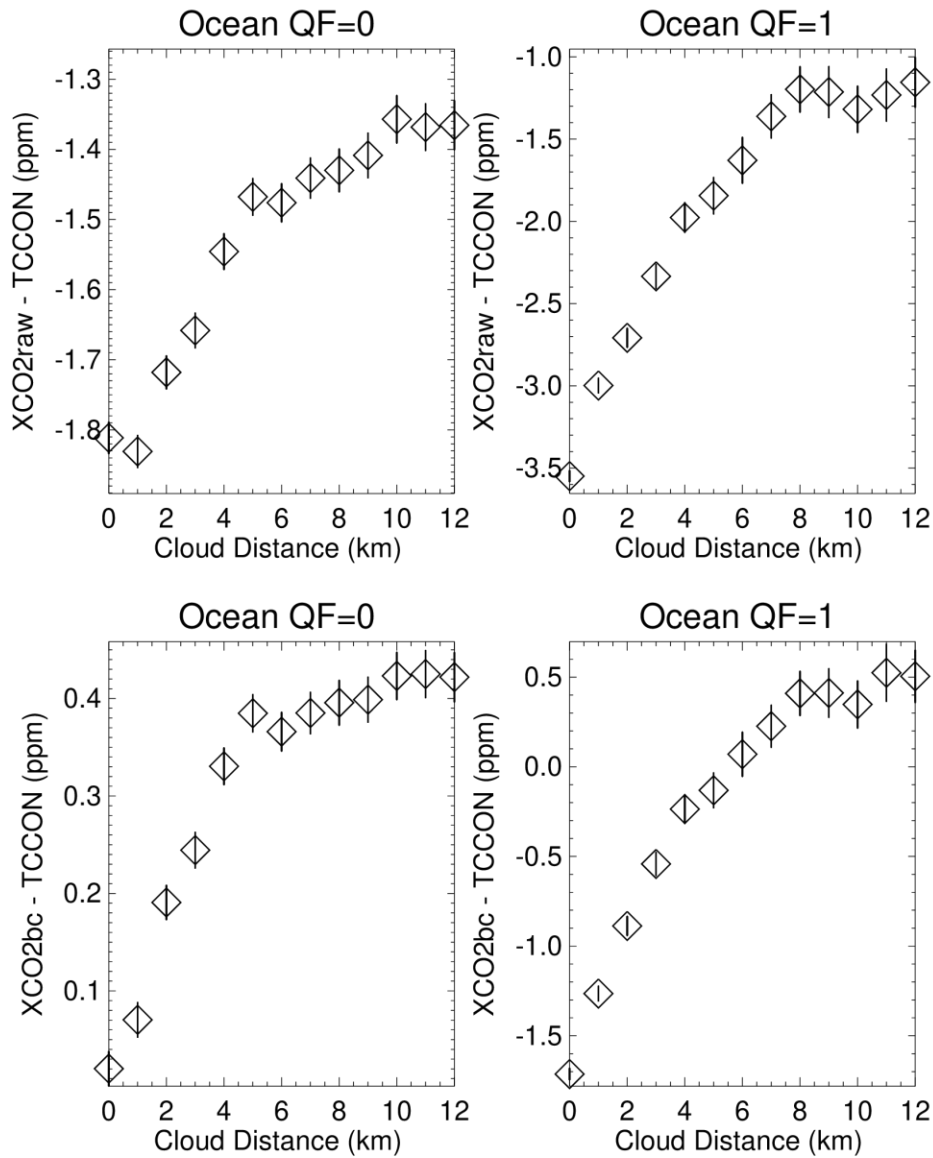
1515   **Figure 6.** Averages of XCO2 – TCCON over the ocean as a function of the nearest cloud distance for QF=0 and QF=1 XCO2raw and XCO2bc Version 10 data. 95 % (2σ) confidence limits of the averages are represented by the vertical line associated with each average. The averages become more negative as the nearest cloud distance decreases. This indicates that the operational bias correction has a non-zero residual 3D cloud bias.

1520
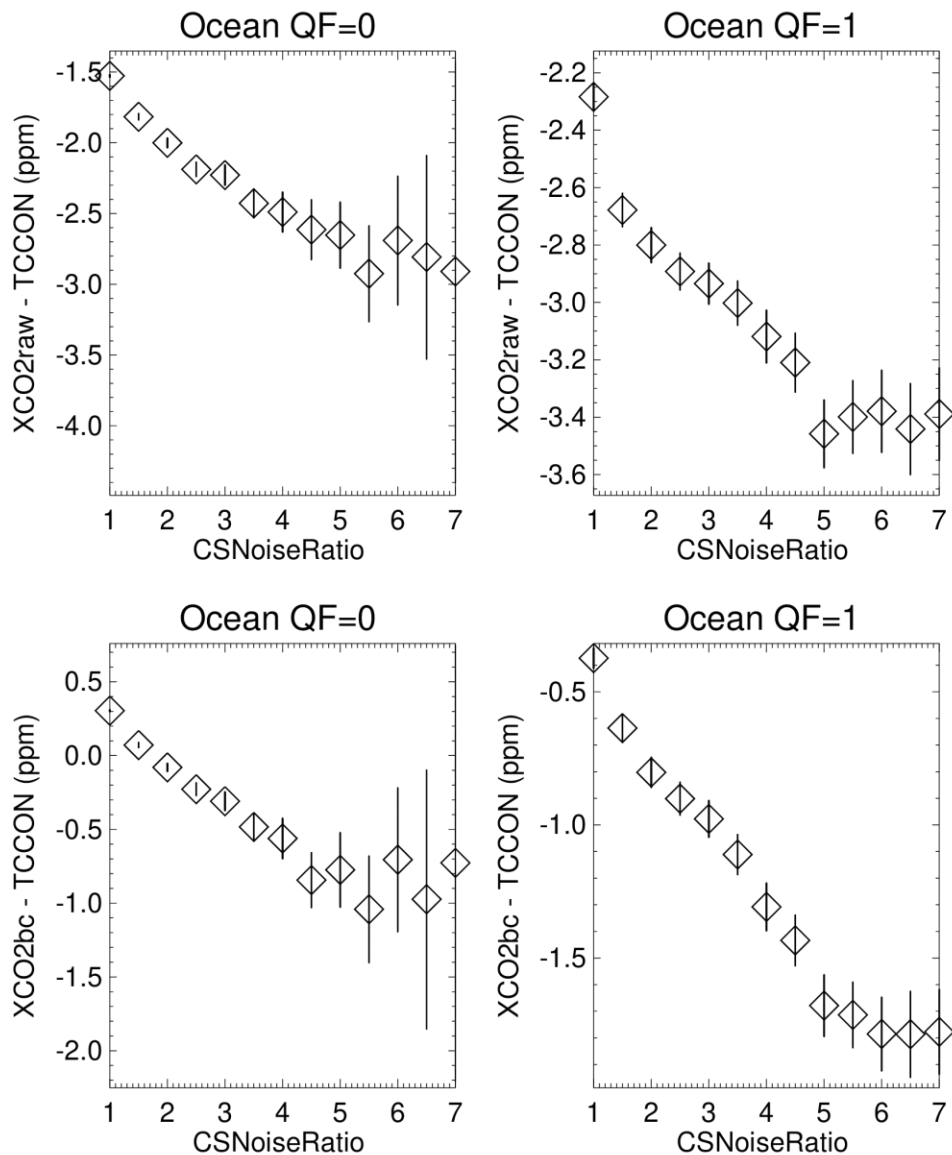
Figure 7. Averages of XCO2 – TCCON over the ocean as a function of the CSNoiseRatio metric for QF=0 and QF=1 XCO2raw and XCO2bc Version 10 data. 95 % (2σ) confidence limits of the averages are represented by the vertical line associated with each average. The averages become more negative for the QF=0 and QF=1 quality flags as the CSNoiseRatio

1525   metric increases.
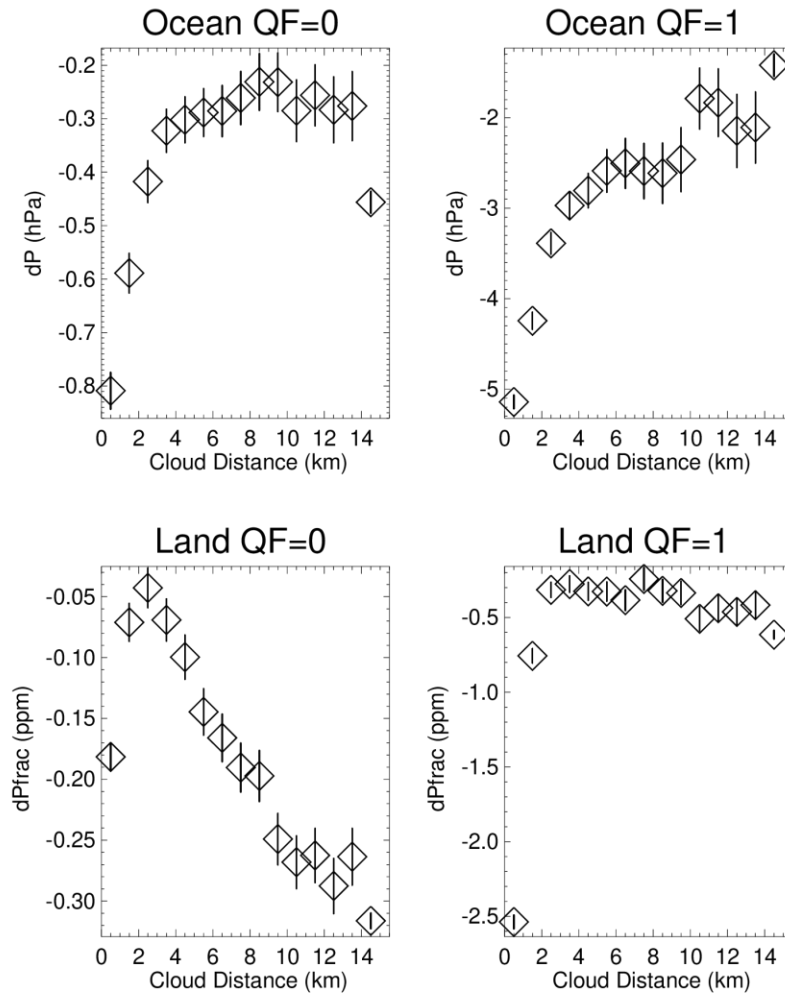
Figure 8. Averages of dPsco2 over the ocean and dPfrac over land as a function of the nearest cloud distance metric for QF=0 and QF=1 Version 10 data. 95 % (2σ) confidence limits of the averages are represented by the vertical line associated with each average.

1530
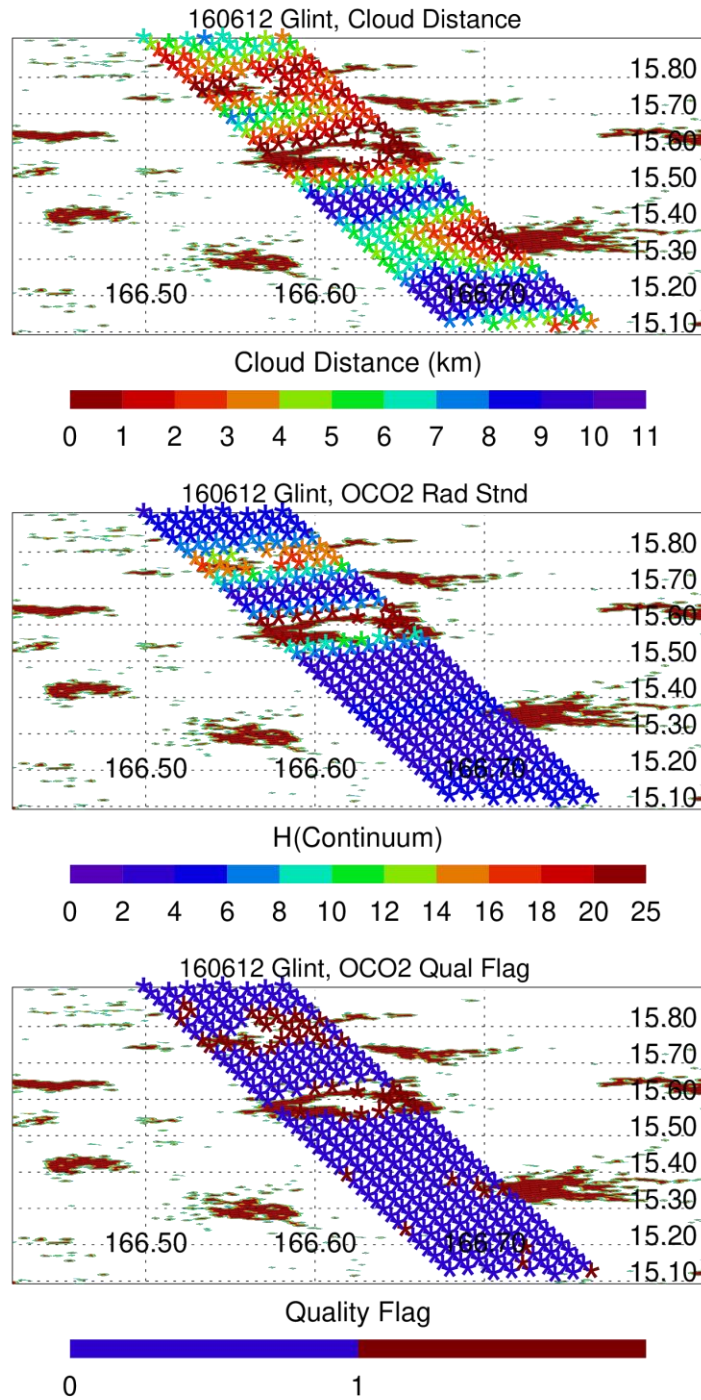
Figure 9. Geospatial variations in nearest cloud distance, O2-Aband continuum H(Continuum), and Quality Flag values for an ocean glint scene on June 12, 2016. Footprint observations are indicated by * symbols, and the MODIS cloud field is given by
1535 the irregular red shapes. Longitude and Latitude are given by the x and y axes.
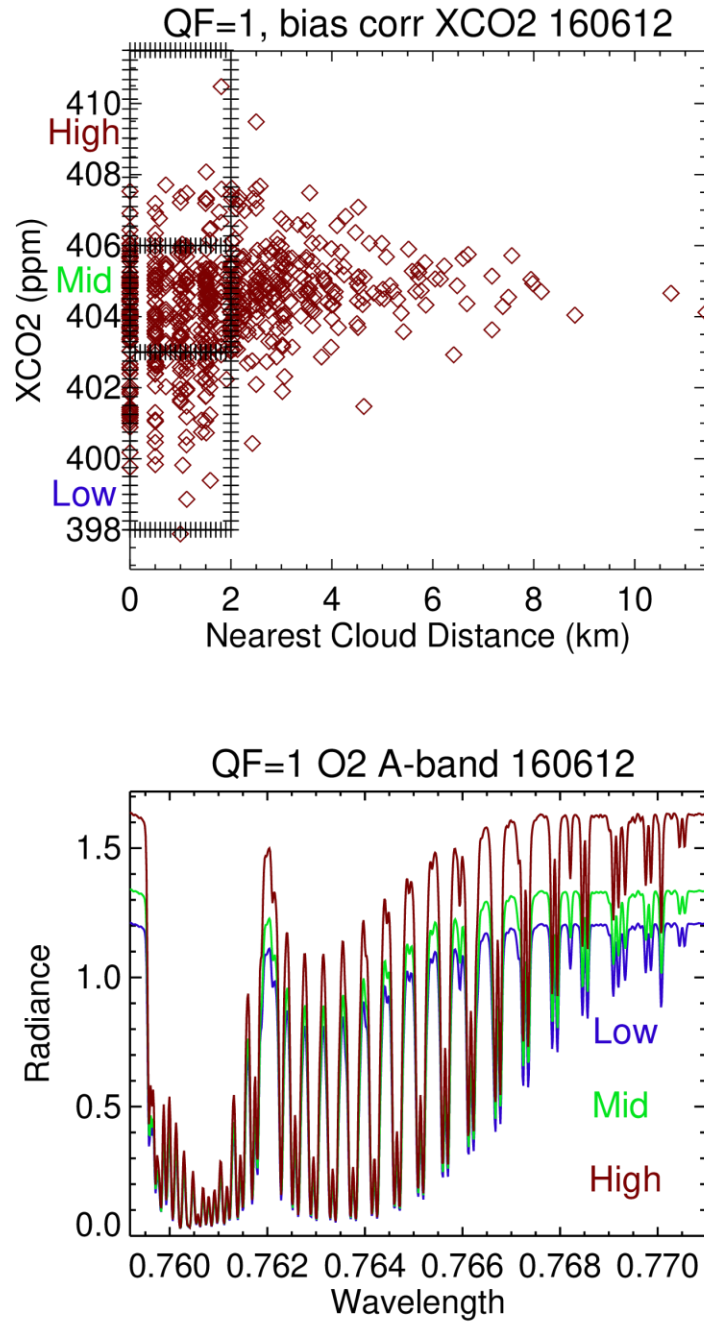
Figure 10. Bias corrected Version 10 XCO2bc versus nearest cloud distance for QF=1 data for a region that extends north and south of the June 12, 2016 scene illustrated in Fig. 9. The bottom panel presents O_2 A-band average spectra for the three boxes in the upper panel.
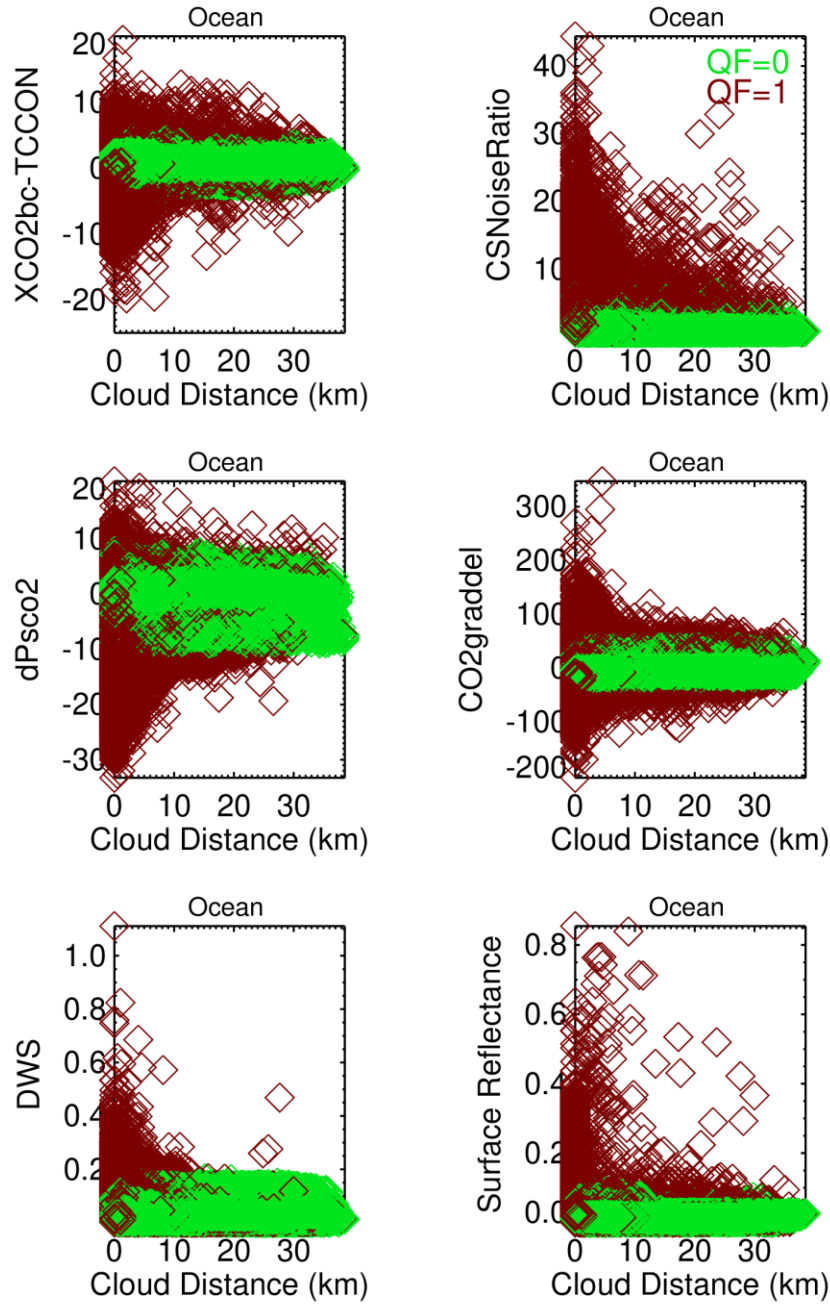
Figure 11. Dependence of Version 10 ocean bias correction variables (dPsco2, CO2graddel) and other variables (DWS, surface reflectance, and CSNoiseRatio) as a function of nearest cloud distance and Quality Flag data. The data points are for a limited range of latitude (52S ° - 41S°) and longitude (164° - 180°) in 2017.
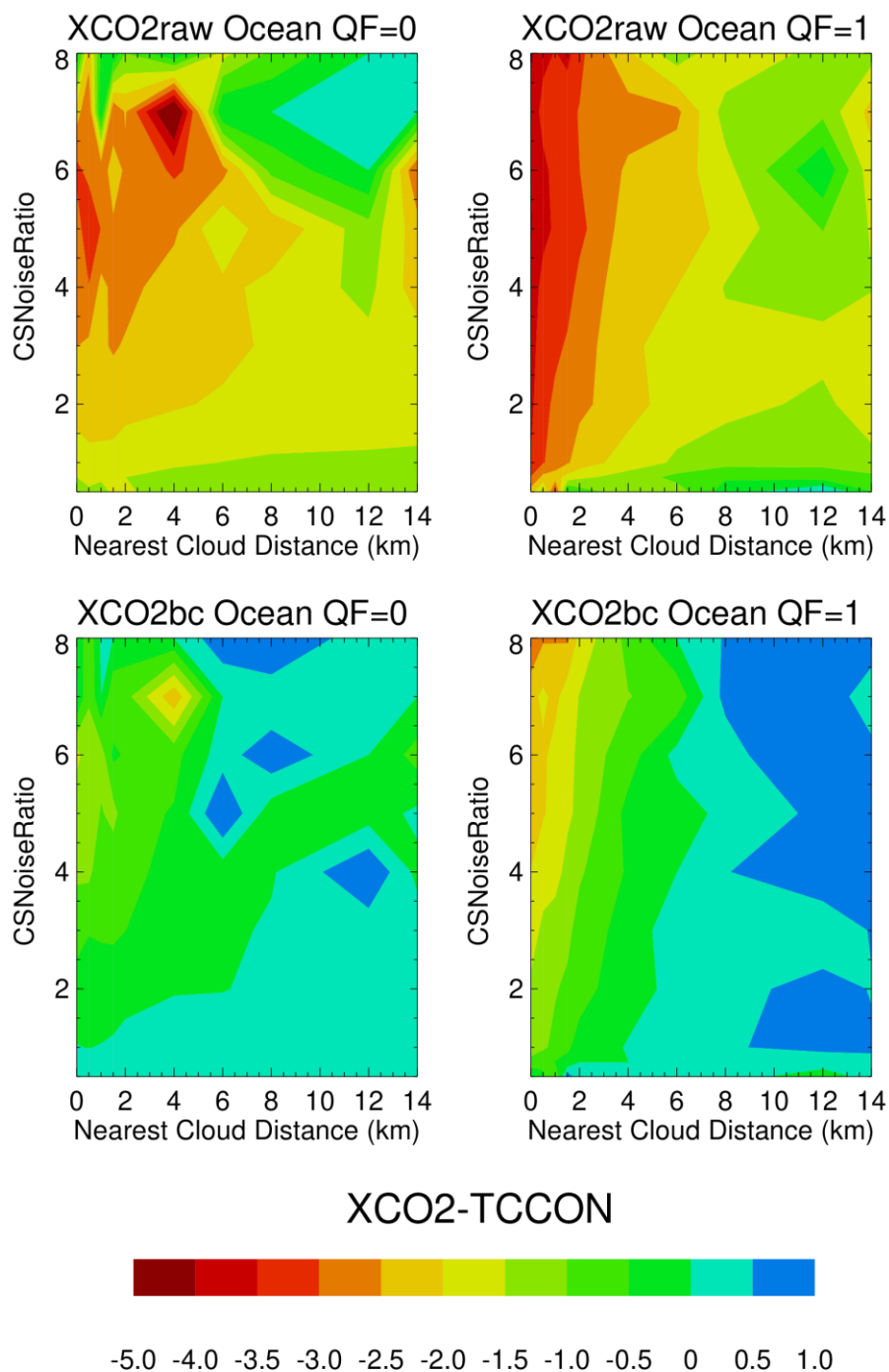
Figure 12. Contour graphs of XCO2raw-TCCON and XCO2bc-TCCON for ocean glint measurements. Largest differences are present at smallest nearest cloud distances and largest CSNoiseRatio values especially for the QF=1 data.
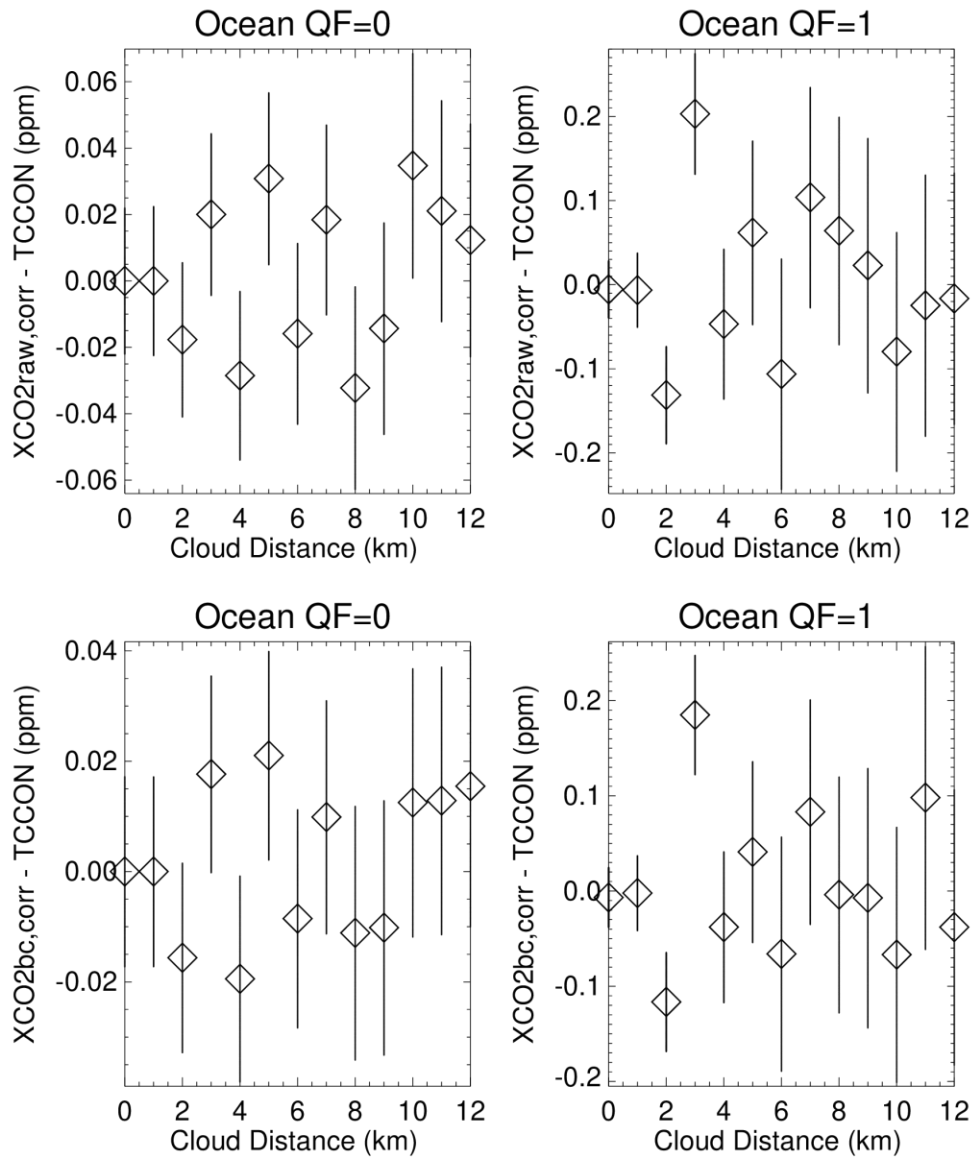
Figure 13. Application of Fig. 12, used as a Table look-up correction for 3D cloud biases, leads to revised XCO2raw,corr-TCCON and XCO2bc,corr-TCCON averages for ocean data, binned as a function of nearest cloud distance.
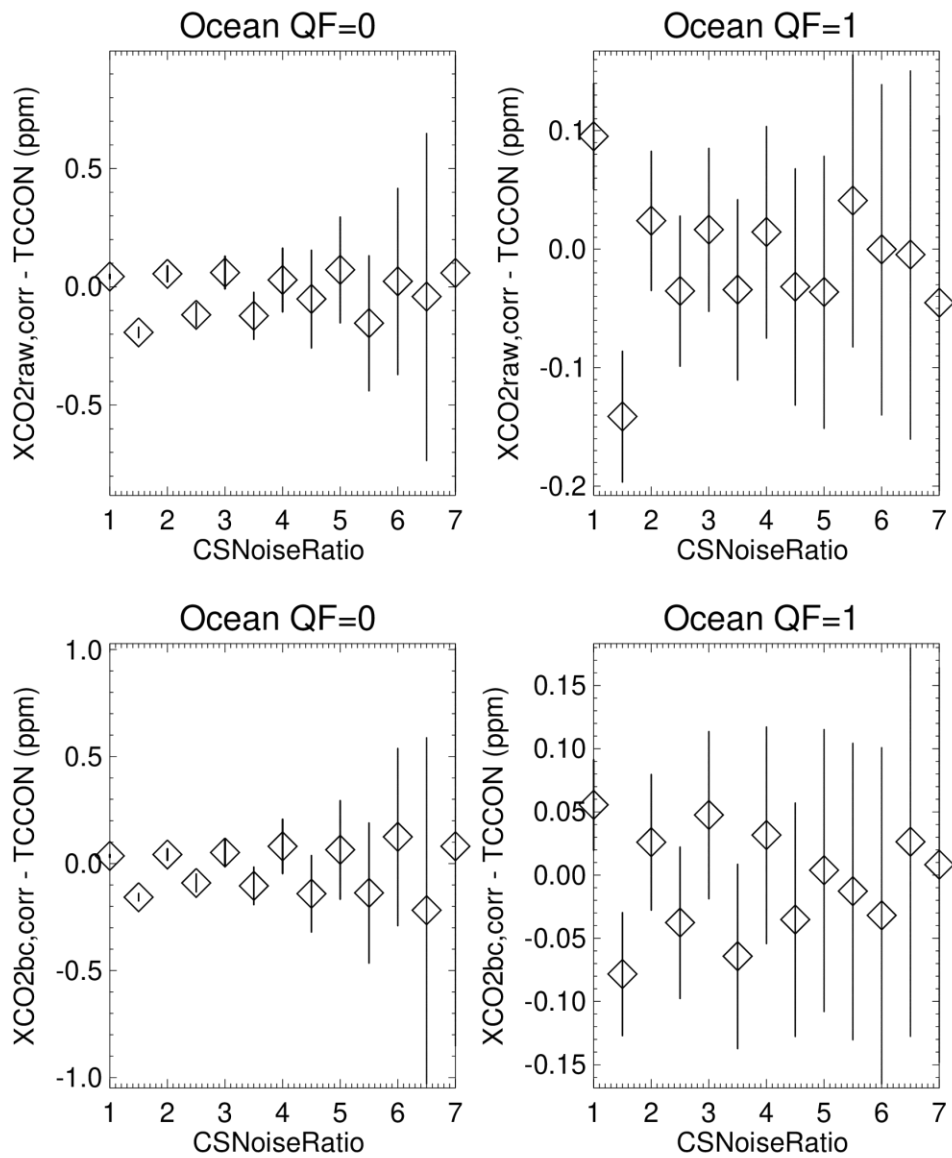
Figure 14. Application of Fig. 12, used as a Table look-up correction for 3D cloud biases, leads to revised XCO2raw,corr-TCCON and XCO2bc,corr-TCCON averages for ocean data, binned as a function of the CSNoiseRatio 3D metric.

1560
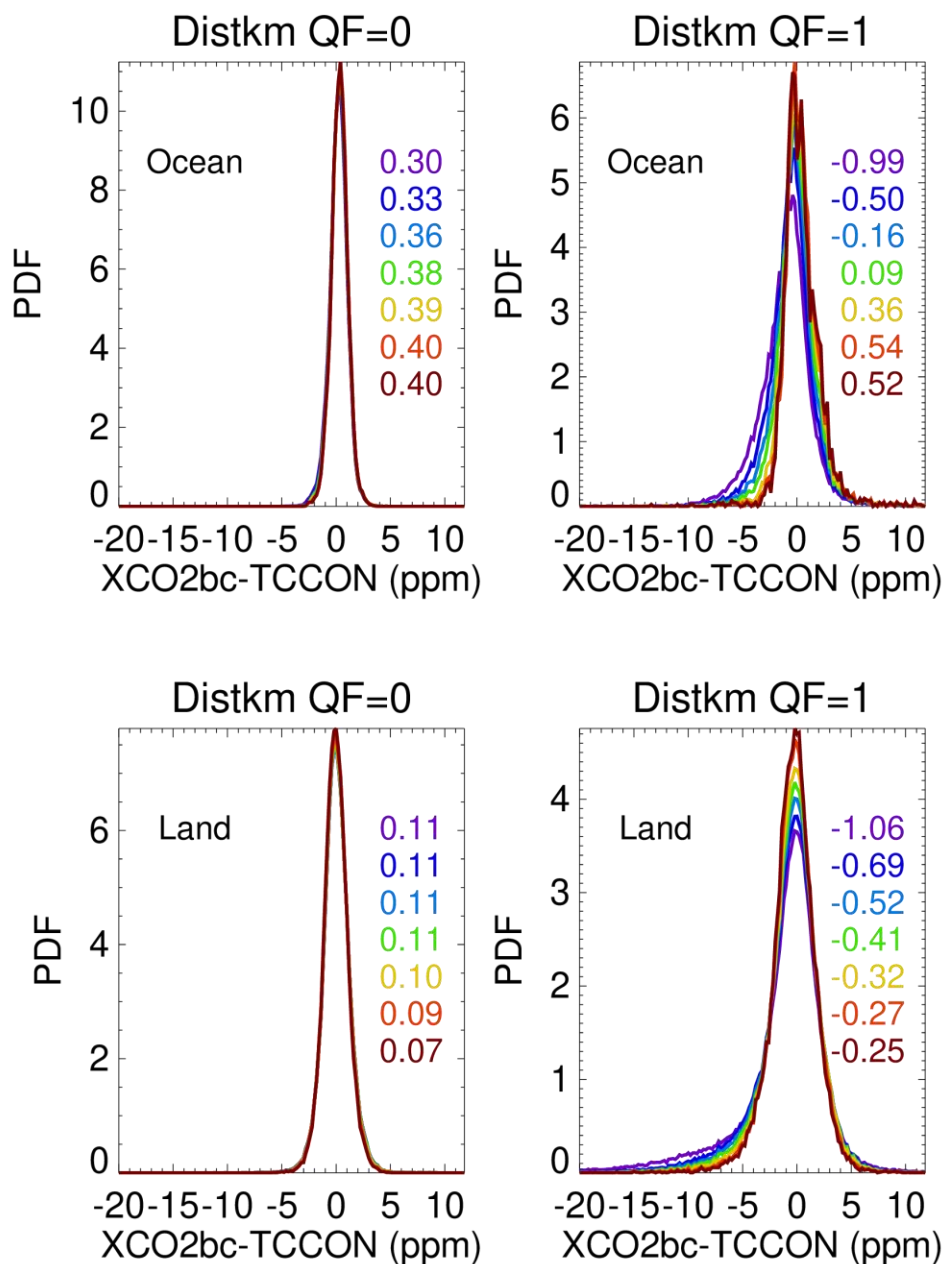
Figure 15. Changes in the PDFs of Version 10 XCO2bc-TCCON as a function of the nearest cloud distance screening process (see Tables 7 and 8). The numbers in the panels are the number weighted XCO2bc-TCCON averages (in ppm) of the PDFs, for nearest cloud screening threshold distances of 0, 1, 2, 3, 5, 10, and 15 km.

1565